Efficient spatial compliance analysis of general initially curved beams for mechanism synthesis and optimization

Ke Wu, Gang Zheng, Guangbo Hao

To cite this version:

Ke Wu, Gang Zheng, Guangbo Hao. Efficient spatial compliance analysis of general initially curved beams for mechanism synthesis and optimization. Mechanism and Machine Theory, 2021, 162, pp.104343. 10.1016/j.mechmachtheory.2021.104343 . hal-03509067

Version of Record: https://www.sciencedirect.com/science/article/pii/S0094114X21001014
Manuscript_7f6fc8a775ff9189438b70b78229273c

Efficient Spatial Compliance Analysis of General Initially Curved Beams for Mechanism Synthesis and Optimization[⋆]

Ke Wu[a], Gang Zheng[a,*] and Guangbo Hao[b]

[a]INRIA Lille-Nord Europe, 40 Avenue Halley, 59650, Villeneuve d'Ascq, France
[b]School of Engineering and Architecture -Electrical and Electronic Engineering, University College Cork, Cork, Ireland

ARTICLE INFO

Keywords:
Compliant Mechanisms
Initially Curved Beams (ICBs)
Compliance Analysis
Optimization
ICB-based Parallelogram
Ortho-planar spring

ABSTRACT

Compliant Mechanisms (CMs) present several desired properties for mechanical designs. Conventional rigid-body mechanisms composed of rigid links connected at kinematic joints, serve as devices to transfer motion, force and energy by the movements of rigid links whereas CMs are able to present the same function only through deflection of flexible members. Most designs of CMs in the current literature employ straight beams as the elementary flexible members whereas initially curved beams (ICBs) also provide potential advantages for CMs such as large range of motion and small strain range. This paper presents an efficient spatial compliance analysis method of general ICBs. The spatial compliance analysis of different types of ICBs (such as varying-curvature beams and varying-cross-section beams) was conducted, followed by Finite Element Analysis (FEA) verification. Next, the modeling and optimization of two types of CMs including ICB-based parallelogram mechanisms and ICB-based Ortho-planar springs were carried out by applying screw theory under the framework of position space concept and parameter normalization strategy where a class of anti-buckling translational parallelograms with high load-bearing capacity and a type of compact 2R1T (2 rotational DOF and 1 translational DOF) compliant kinematic joints were obtained. The corresponding FEA was conducted to verify the optimal results.

1. Introduction

As a promising alternative of designing mechanical systems, Compliant Mechanisms (CMs) provide several great solutions for many existing mechanical applications and have become a research hot spot over the last few decades [1]. Conventional mechanisms composed of rigid links attached at kinematic pairs, serve as devices to transfer motion, force and energy by the translational and angular movements of a group of physically interrelated rigid links while CMs are able to do the same only counting on the deformation of flexible members [1][2]. CMs have already demonstrated many meaningful advantages over conventional rigid–body mechanisms, including increased motion precision [3][4][5][6][7][8][9], simplified manufacturing process [1][2][3], reduced weight [1][2], cost reduction [1][2][3] and less maintenance [1][2]. Owing to the mentioned merits, many great designs that employ CMs have been proposed for a wide variety of practical applications, such as compliant kinematic joints [10][11][12][13], positioning motion stage [4][5][8][9][14][15], actuators [16][17][18][19] and sensors [19][20]. However, most of the mentioned studies above only employ straight beams as the elementary flexible members, and straight beams have been maturely studied in terms of spatial compliance synthesis of CMs [21].

Initially curved beams (ICBs) have also demonstrated their potential advantages. Some decent applications integrating ICBs have been reported in the literature: the contributors of [22] proposed an optimization-based systematic synthesis for path-generating CMs using ICBs, in which ICBs display diverse mechanical properties; ICBs are also a good alternative that can be integrated for designing bi-stable or multi-stable CMs [23][24][25][26][27]; due to its relatively large deflection range and relatively small strain range, ICBs have been used as the elementary flexible members to design compliant kinematic joints and positioning stage for transferring displacements and forces [28][29][30][31][32][33][34], and these properties are also desired in civil, aerospace and electronic engineering respectively [35][36][37].

Although ICBs are commonly employed in CMs, the studies on characterizing and analyzing such beams are rather limited: Pseudo-rigid-body (PRB) assumptions are a popular option to analyze large deformation of curved

---

[⋆] This research was supported by INRIA Lille-Nord Europe
[*] Corresponding author. Email: gang.zheng@inria.fr
ORCID(s):

beams [27][38][39][40]; [41] developed a generalized Beam Constraint Model (BCM) for modeling 2-D ICBs within intermediate deflection range, based on which [42] presented Chained Beam Constraint Model (CBCM) for modeling large deflection of curved beams; [37] used a direct integration method to characterize stiffness matrices of general spatial/planar curved beams, serving as quite a universal method of obtaining compliance matrix of any type of curved beams; using the same method as [37], [30][31][32] conducted spatial compliance analysis of circularly curved beams whereas they did not consider curvature-varying curved beams and cross-section-varying beams. The above mentioned methods have all presented their effectiveness in modeling ICBs but they also have limitations in terms of different modeling purposes: the superiority of PRB models is transforming compliant mechanisms into equivalent rigid-body mechanisms, which facilitates the use of the wealth of existing rigid-body mechanics knowledge for the solution of compliant mechanisms [43], whereas its limited accuracy in some cases comes from its 'pseudo' modeling nature. [27][38][39][40][41][42] focus on 2-D load-displacement relationship so that they are not able to capture out-of-plane deflection of curved beams; [41][42] mainly concentrate on nonlinear or large-deflection modeling by numerical solutions, which is not suitable for linear compliance analysis through developing explicit analytical formulas. Although the authors of [37] provide a method of conducting spatial linear compliance analysis of ICBs under integration scheme, in this paper we would like to propose a more easy-to-follow and efficient method of analyzing spatial compliance of general ICBs from an energy-based point of view (Maxwell–Mohr Method).

This paper is mainly composed of two parts: we first recalled the definition of general planar curves (in polar coordinate system) and spatial compliance matrix of flexible members, and then derived compliance matrix of general ICBs using Maxwell–Mohr Method under the combined framework of the polar coordinate system and Cartesian coordinate system, followed by FEA verification where three representative beams (a Archimedean-spiral curved beam with a constant square cross-section, a circular curved beam with a constant round cross-section and a circular curved beam with a uniformly varying rectangular cross-section) were studied. In terms of the second part of the paper, we conducted compliance synthesis and geometric optimization of ICB-based parallelogram and ICB-based Ortho-planar spring where based on position space concept [4] and weighted-sum method [44], we improved the mechanical performance of the studied mechanisms, effectively dealing with multi-objectives and multi-variables, where a class of anti-buckling translational parallelograms with high load-bearing capacity and a type of compact 2R1T (2 rotational DOF and 1 translational DOF) compliant kinematic joints were obtained. The optimal results were also verified by FEA. For manufacturing feasibility and engineering purposes, planar ICBs are considered in this paper but the method is not limited to planar beams and can be applied to spatial ICBs as well.

2. Geometric Definition of General Initially Curved Beams

In this section, we aim to geometrically define general ICBs through introducing the polar coordinate system. As demonstrated in [45], it's a two-dimensional coordinate system where every point on the plane is determined by a distance from the pole O (radial coordinate r) and an angle from the polar axis $\overrightarrow{OA}$ (angular coordinate θ) displayed in Fig. 1 where an arbitrary point, such as point B, can be defined by r and θ. Logically, an arbitrary curve can be

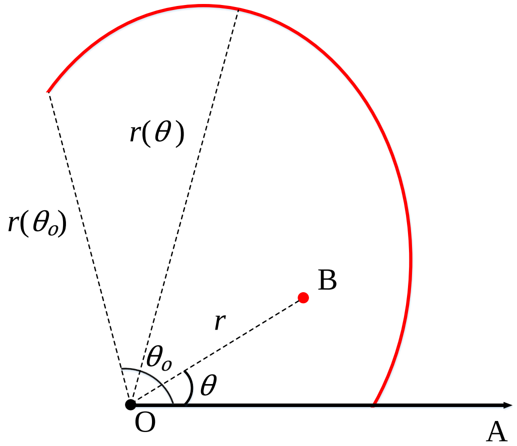

Figure 1: Polar coordinate system for defining points and curves

defined by a function of θ in the polar coordinate system (Fig. 1):

$$r = r(\theta),\ \theta \in [0, \theta_o] \tag{1}$$

Therefore, (1) can be used to define the axis of a general ICB.

3. Compliance Matrix of General Initially Curved Beams

In this section, we mainly focus on deriving free-end spatial compliance matrices of general ICBs using Maxwell–Mohr Method under the combined framework of the polar coordinate system and Cartesian coordinate system.

3.1. Formation of Compliance Matrix

For an arbitrary ICB (Fig. 2), F_x, F_y, F_z, M_x, M_y and M_z stand for the actual loads exerted at the free-end center, resulting in translational and angular displacements. F_x, F_y and F_z are the forces along X, Y and Z axes respectively of its local coordinate system. Similarly, M_x, M_y and M_z denote the bending moments with respect to X, Y and Z axes of its local coordinate system respectively. x, y and z are the translational displacements of the free-end center along X, Y and Z axes respectively. Similar to straight beams, the classic form of free-end spatial compliance matrix $C_S \in \mathbb{R}^{6\times6}$ of a curved flexible member is demonstrated in Eq. 2:

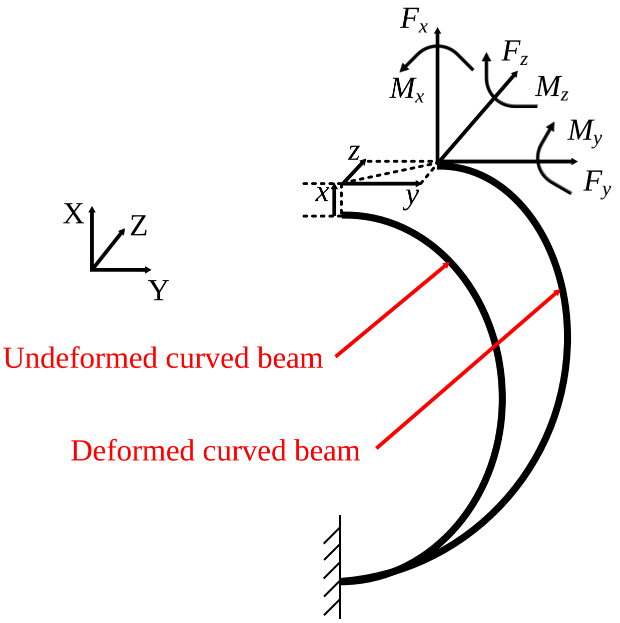

Figure 2: Spatial deformation of an initial curved beam

$$C_S = \begin{bmatrix} c_{s11} & c_{s12} & c_{s13} & c_{s14} & c_{s15} & c_{s16} \\ c_{s21} & c_{s22} & c_{s23} & c_{s24} & c_{s25} & c_{s26} \\ c_{s31} & c_{s32} & c_{s33} & c_{s34} & c_{s35} & c_{s36} \\ c_{s41} & c_{s42} & c_{s43} & c_{s44} & c_{s45} & c_{s46} \\ c_{s51} & c_{s52} & c_{s53} & c_{s54} & c_{s55} & c_{s56} \\ c_{s61} & c_{s62} & c_{s63} & c_{s64} & c_{s65} & c_{s66} \end{bmatrix} = \begin{bmatrix} \frac{\partial x}{\partial F_x} & \frac{\partial x}{\partial F_y} & \frac{\partial x}{\partial F_x} & \frac{\partial x}{\partial M_x} & \frac{\partial x}{\partial M_y} & \frac{\partial x}{\partial M_z} \\ \frac{\partial y}{\partial F_x} & \frac{\partial y}{\partial F_y} & \frac{\partial y}{\partial F_x} & \frac{\partial y}{\partial M_x} & \frac{\partial y}{\partial M_y} & \frac{\partial y}{\partial M_z} \\ \frac{\partial z}{\partial F_x} & \frac{\partial z}{\partial F_y} & \frac{\partial z}{\partial F_x} & \frac{\partial z}{\partial M_x} & \frac{\partial z}{\partial M_y} & \frac{\partial z}{\partial M_z} \\ \frac{\partial \theta_x}{\partial F_x} & \frac{\partial \theta_x}{\partial F_y} & \frac{\partial \theta_x}{\partial F_x} & \frac{\partial \theta_x}{\partial M_x} & \frac{\partial \theta_x}{\partial M_y} & \frac{\partial \theta_x}{\partial M_z} \\ \frac{\partial \theta_y}{\partial F_x} & \frac{\partial \theta_y}{\partial F_y} & \frac{\partial \theta_y}{\partial F_x} & \frac{\partial \theta_y}{\partial M_x} & \frac{\partial \theta_y}{\partial M_y} & \frac{\partial \theta_y}{\partial M_z} \\ \frac{\partial \theta_z}{\partial F_x} & \frac{\partial \theta_z}{\partial F_y} & \frac{\partial \theta_z}{\partial F_x} & \frac{\partial \theta_z}{\partial M_x} & \frac{\partial \theta_z}{\partial M_y} & \frac{\partial \theta_z}{\partial M_z} \end{bmatrix} \tag{2}$$

which is essentially a Jacobian matrix explaining the force-displacement relationship in small deformations in Eq. 3:

$$D = C_S F \tag{3}$$

where $F \in \mathbb{R}^{6\times1}$ denotes the force vector exerted at the beam tip and $D \in \mathbb{R}^{6\times1}$ stands for the free-end displacement vector in Eq. 4:

$$D = \begin{bmatrix} x & y & z & \theta_x & \theta_y & \theta_z \end{bmatrix}^T, F = \begin{bmatrix} F_x & F_y & F_z & M_x & M_y & M_z \end{bmatrix}^T \tag{4}$$

3.2. Derivation of Compliance Matrix

Unlike the free-end compliance of straight beams [21], ICBs display more diverse mechanical properties [22], which is therefore more difficult to be spatially modeled. Maxwell–Mohr Method is introduced and recalled here to derive all elements in C_S since it's a universal method for computing displacements at any point of any flexible member. Besides, Maxwell–Mohr method also allows calculating mutual displacements, whose general mathematical expression is written in Eq. 5:

$$\Delta_{kp} = \sum \int_0^s \frac{M_p \cdot \bar{m}_k}{EI_m} \mathrm{d}s + \sum \int_0^s \frac{F_p \cdot \bar{f}_k}{EA} \mathrm{d}s + \sum \int_0^s \frac{T_p \cdot \bar{t}_k}{GI_p} \mathrm{d}s \tag{5}$$

which implies that displacements caused by any combination of loads can be expressed utilizing internal forces developed by given loads and unit load (which corresponds to required displacement). All symbols in (Eq. 5) are explained as follows: Δ_{kp} denotes the displacement of a flexible member in the k direction under p condition (p-direction loading); M_p, F_p and T_p are the internal forces (bending moment, force and torque) due to the given bending moment, axial force and torque respectively; $\bar{m}_k$, $\bar{f}_k$ and $\bar{t}_k$ are the internal bending moment, axial force and torque respectively of an arbitrary section of the given flexible member under a unit load; E and G denote the Young's modulus and the Shear modulus of the material respectively; A is the cross-section area of the given flexible member; I_m and I_p denote the second moment of the area of the cross section and polar moment of inertia of the cross section respectively.

Based on the recalling above, we would like to conduct spatial compliance analysis of general ICBs. The general loading conditions of a flexible curved member (the red curve: $r = r(\theta)$, $\theta \in [0, \theta_o]$) for compliance analysis of X-Y plane are graphically displayed in Fig. 3 depending on the combined structure of the polar coordinate system and Cartesian coordinate system, which is utilized to assist in deriving its spatial compliance matrix C_S. As demonstrated in Fig. 3, F_x, F_y, F_z, M_x, M_y and M_z denote the actual loads exerted at the free end of the curved beam; $\bar{f}_x$, $\bar{f}_y$, $\bar{f}_z$, $\bar{m}_x$, $\bar{m}_y$ and $\bar{m}_z$ are the internal forces due to the unit loads in the corresponding directions; d_x is the force arm of F_x and $\bar{f}_x$ with respect to ds and similarly d_y is the force arm of F_y and $\bar{f}_y$ with respect to ds where d_x and d_y are functions of $r(\theta)$ and θ developed in Cartesian coordinate system (Eq. 6):

$$\begin{aligned} d_x &= \begin{bmatrix} 0 & r(\theta)\sin(\theta) - r(\theta_o)\sin(\theta_o) & 0 \end{bmatrix}^T \\ d_y &= \begin{bmatrix} r(\theta)\cos(\theta) - r(\theta_o)\cos(\theta_o) & 0 & 0 \end{bmatrix}^T \end{aligned} \tag{6}$$

$\hat{u}_t$ is the unit tangent vector at ds pointing to the growth direction of the curve and $\hat{u}_n$ is the inward-pointing unit normal vector at ds (see Fig. 3 and Fig. 4) where $\hat{u}_t$ and $\hat{u}_n$ are functions of $r(\theta)$ and θ developed in Cartesian coordinate system as well (Eq. 7):

$$\begin{aligned} \hat{u}_t &= \frac{\begin{bmatrix} \frac{\mathrm{d}r(\theta)}{\mathrm{d}\theta}\cos(\theta) - r(\theta)\sin(\theta) & \frac{\mathrm{d}r(\theta)}{\mathrm{d}\theta}\sin(\theta) + r(\theta)\cos(\theta) & 0 \end{bmatrix}^T}{\left\| \begin{bmatrix} \frac{\mathrm{d}r(\theta)}{\mathrm{d}\theta}\cos(\theta) - r(\theta)\sin(\theta) & \frac{\mathrm{d}r(\theta)}{\mathrm{d}\theta}\sin(\theta) + r(\theta)\cos(\theta) & 0 \end{bmatrix} \right\|} \\ \hat{u}_n &= \frac{\begin{bmatrix} \frac{\mathrm{d}r(\theta)}{\mathrm{d}\theta}\sin(\theta) + r(\theta)\cos(\theta) & -(\frac{\mathrm{d}r(\theta)}{\mathrm{d}\theta}\cos(\theta) - r(\theta)\sin(\theta)) & 0 \end{bmatrix}^T}{\left\| \begin{bmatrix} \frac{\mathrm{d}r(\theta)}{\mathrm{d}\theta}\sin(\theta) + r(\theta)\cos(\theta) & -(\frac{\mathrm{d}r(\theta)}{\mathrm{d}\theta}\cos(\theta) - r(\theta)\sin(\theta)) & 0 \end{bmatrix} \right\|} \end{aligned} \tag{7}$$

B is an arbitrary point on the curve and C is the beam tip; the lengths of $\overline{\mathrm{OB}}$ and $\overline{\mathrm{OC}}$ can be represented by $r(\theta)$ and $r(\theta_o)$ respectively where point O is the origin of the polar coordinate system and Cartesian coordinate system; ds can be expressed by $r(\theta)$ and θ (Eq. 8):

$$\mathrm{d}s = \sqrt{r(\theta)^2 + (\frac{\mathrm{d}r(\theta)}{\mathrm{d}\theta})^2}\, \mathrm{d}\theta \tag{8}$$

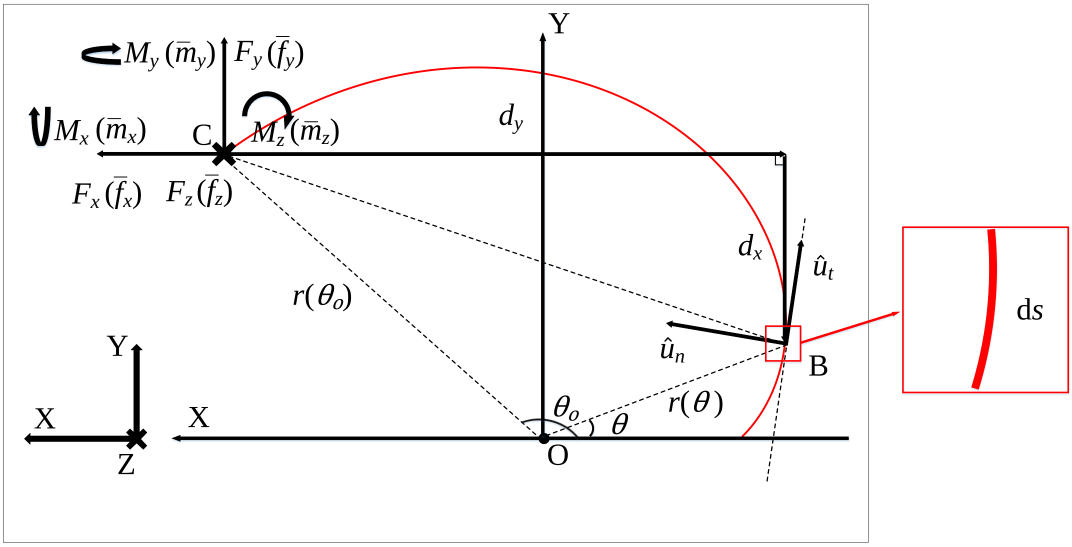

Figure 3: Loading conditions of an ICB for compliance analysis in X-Y plane

Therefore, we have:

$$c_{s11} = \int_0^{\theta_o} \frac{(F_x \times d_x)\cdot(\bar{f}_x \times d_x)}{|F_x||\bar{f}_x|EI_{mz}}\mathrm{d}s + \int_0^{\theta_o} \frac{[(F_x \cdot \hat{u}_t)\hat{u}_t]\cdot[(\bar{f}_x \cdot \hat{u}_t)\hat{u}_t]}{|F_x||\bar{f}_x|EA}\mathrm{d}s \tag{9}$$

$$c_{s21} = c_{s12} = \int_0^{\theta_o} \frac{(F_x \times d_x)\cdot(\bar{f}_y \times d_y)}{|F_x||\bar{f}_y|EI_{mz}}\mathrm{d}s + \int_0^{\theta_o} \frac{[(F_x \cdot \hat{u}_t)\hat{u}_t]\cdot[(\bar{f}_y \cdot \hat{u}_t)\hat{u}_t]}{|F_x||\bar{f}_y|EA}\mathrm{d}s \tag{10}$$

$$c_{s61} = c_{s16} = \int_0^{\theta_o} \frac{(F_x \times d_x)\cdot(\bar{m}_z)}{|F_x||\bar{m}_z|EI_{mz}}\mathrm{d}s \tag{11}$$

$$c_{s22} = \int_0^{\theta_o} \frac{(F_y \times d_y)\cdot(\bar{f}_y \times d_y)}{|F_y||\bar{f}_y|EI_{mz}}\mathrm{d}s + \int_0^{\theta_o} \frac{[(F_y \cdot \hat{u}_t)\hat{u}_t]\cdot[(\bar{f}_y \cdot \hat{u}_t)\hat{u}_t]}{|F_y||\bar{f}_y|EA}\mathrm{d}s \tag{12}$$

$$c_{s62} = c_{s26} = \int_0^{\theta_o} \frac{(F_y \times d_y)\cdot(\bar{m}_z)}{|F_y||\bar{m}_z|EI_{mz}}\mathrm{d}s \tag{13}$$

$$c_{s66} = \int_0^{\theta_o} \frac{M_z \cdot(\bar{m}_z)}{|M_z||\bar{m}_z|EI_{mz}}\mathrm{d}s \tag{14}$$

The above Eq. 9 to 14 define the 9 elements in the compliance matrix C_S which represent the compliance of X-Y plane deformation where I_{mz} is the second moment of the area of the cross section with respect to Z axis (see Fig. 4).

The following focuses on compliance of out-of-plane deformation displayed in Fig. 4: $\overline{\mathrm{CM}}$ is constructed to be perpendicular to $\overleftrightarrow{\mathrm{BM}}$ (which is the tangent line to the curve at point B) intersecting at point M; d_{z_n} is the normal force arm of F_z and $\bar{f}_z$ with respect to point B, and its direction is from point C to point M; d_{z_t} is the tangent force arm of

F_z and $\bar{f}_z$ with respect to point B, and its direction is from point M to point B; d_{z_n} and d_{z_t} are also functions of $r(\theta)$ and θ developed in Cartesian coordinate system (Eq. 15):

$$\begin{bmatrix} X_M(\theta) \\ Y_M(\theta) \end{bmatrix} = \begin{bmatrix} \frac{\frac{\mathrm{d}r(\theta)}{\mathrm{d}\theta}\cos(\theta)-r(\theta)\sin(\theta)}{\frac{\mathrm{d}r(\theta)}{\mathrm{d}\theta}\sin(\theta)+r(\theta)\cos(\theta)} & 1 \\ -\frac{\frac{\mathrm{d}r(\theta)}{\mathrm{d}\theta}\sin(\theta)+r(\theta)\cos(\theta)}{\frac{\mathrm{d}r(\theta)}{\mathrm{d}\theta}\cos(\theta)-r(\theta)\sin(\theta)} & 1 \end{bmatrix}^{-1} \begin{bmatrix} r(\theta_o)\sin(\theta_o) + \frac{\frac{\mathrm{d}r(\theta)}{\mathrm{d}\theta}\cos(\theta)-r(\theta)\sin(\theta)}{\frac{\mathrm{d}r(\theta)}{\mathrm{d}\theta}\sin(\theta)+r(\theta)\cos(\theta)} r(\theta_o)\cos(\theta_o) \\ r(\theta)\sin(\theta) - \frac{\frac{\mathrm{d}r(\theta)}{\mathrm{d}\theta}\sin(\theta)+r(\theta)\cos(\theta)}{\frac{\mathrm{d}r(\theta)}{\mathrm{d}\theta}\cos(\theta)-r(\theta)\sin(\theta)} r(\theta)\cos(\theta) \end{bmatrix}$$

$$d_{z_t} = \begin{bmatrix} r(\theta)\cos(\theta) - X_M(\theta) & r(\theta)\sin(\theta) - Y_M(\theta) & 0 \end{bmatrix}^T$$

$$d_{n_t} = \begin{bmatrix} X_M(\theta) - r(\theta_o)\cos(\theta_o) & Y_M(\theta) - r(\theta_o)\sin(\theta_o) & 0 \end{bmatrix}^T \tag{15}$$

where $X_M(\theta)$ and $Y_M(\theta)$ are the Cartesian coordinates of point M.

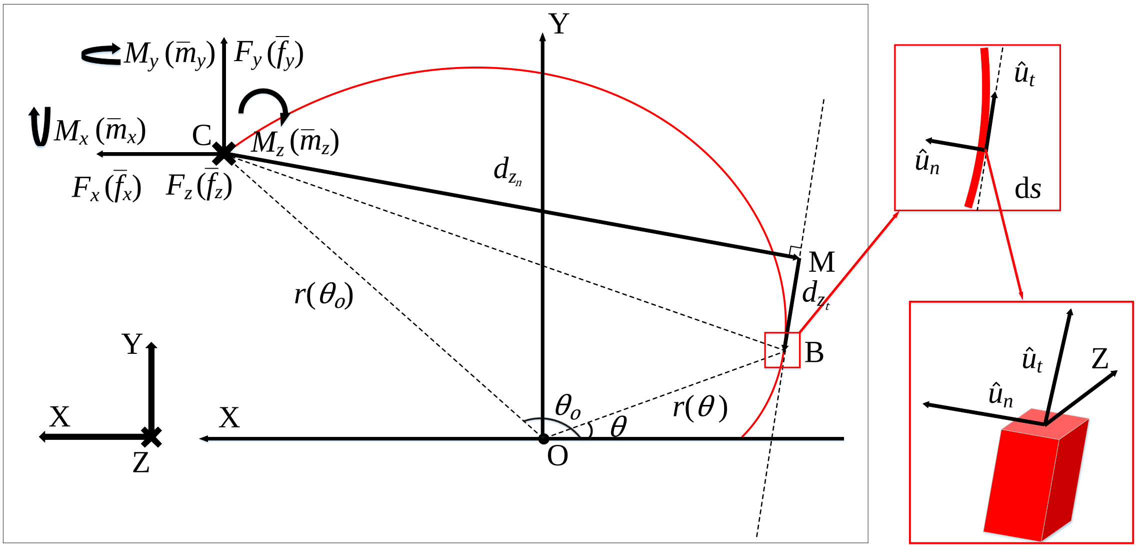

Figure 4: Loading conditions of an ICB for out-of-plane compliance analysis

$$c_{s33} = \int_0^{\theta_o} \frac{(F_z \times d_{z_t}) \cdot (\bar{f}_z \times d_{z_t})}{EI_{m_{\hat{u}_n}} |F_z||\bar{f}_z|} \mathrm{d}s + \int_0^{\theta_o} \frac{(F_z \times d_{z_n}) \cdot (\bar{f}_z \times d_{z_n})}{GI_p |F_z||\bar{f}_z|} \mathrm{d}s \tag{16}$$

$$c_{s43} = c_{s34} = \int_0^{\theta_o} \frac{(F_z \times d_{z_t}) \cdot \bar{m}_x}{EI_{m_{\hat{u}_n}} |F_z||\bar{m}_x|} \mathrm{d}s + \int_0^{\theta_o} \frac{(F_z \times d_{z_n}) \cdot \bar{m}_x}{GI_p |F_z||\bar{m}_x|} \mathrm{d}s \tag{17}$$

$$c_{s53} = c_{s35} = \int_0^{\theta_o} \frac{(F_z \times d_{z_t}) \cdot \bar{m}_y}{EI_{m_{\hat{u}_n}} |F_z||\bar{m}_y|} \mathrm{d}s + \int_0^{\theta_o} \frac{(F_z \times d_{z_n}) \cdot \bar{m}_y}{GI_p |F_z||\bar{m}_y|} \mathrm{d}s \tag{18}$$

$$c_{s44} = \int_0^{\theta_o} \frac{[(M_x \cdot \hat{u}_n)\hat{u}_n] \cdot [(\bar{m}_x \cdot \hat{u}_n)\hat{u}_n]}{EI_{m_{\hat{u}_n}} |M_x||\bar{m}_x|} \mathrm{d}s + \int_0^{\theta_o} \frac{[(M_x \cdot \hat{u}_t)\hat{u}_t] \cdot [(\bar{m}_x \cdot \hat{u}_t)\hat{u}_t]}{GI_p |M_x||\bar{m}_x|} \mathrm{d}s \tag{19}$$

$$c_{s54} = c_{s45} = \int_0^{\theta_o} \frac{[(M_x \cdot \hat{u}_n)\hat{u}_n] \cdot [(\bar{m}_y \cdot \hat{u}_n)\hat{u}_n]}{EI_{m_{\hat{u}_n}} |M_x||\bar{m}_y|} \mathrm{d}s + \int_0^{\theta_o} \frac{[(M_x \cdot \hat{u}_t)\hat{u}_t] \cdot [(\bar{m}_y \cdot \hat{u}_t)\hat{u}_t]}{GI_p |M_x||\bar{m}_y|} \mathrm{d}s \tag{20}$$

$$c_{s55} = \int_0^{\theta_o} \frac{[(M_y \cdot \hat{u}_n)\hat{u}_n] \cdot [(\bar{m}_y \cdot \hat{u}_n)\hat{u}_n]}{EI_{m_{\hat{u}_n}} |M_y||\bar{m}_y|} \mathrm{d}s + \int_0^{\theta_o} \frac{[(M_y \cdot \hat{u}_t)\hat{u}_t] \cdot [(\bar{m}_y \cdot \hat{u}_t)\hat{u}_t]}{GI_p |M_y||\bar{m}_y|} \mathrm{d}s \tag{21}$$

Eq. 16 to Eq. 21 are used to define the 9 elements that denote the compliance of out-of-plane deformation where $I_{m_{\hat{u}_n}}$ denotes the second moment of the area of the cross section with respect to its corresponding unit normal vector $\hat{u}_n$ (see Fig. 4). The values of the rest elements using Eq. 5 are obtained in Eq. 22:

$$\begin{aligned} &c_{s31} = c_{s41} = c_{s51} = c_{s32} = c_{s42} = c_{s52} = c_{s13} = c_{s23} = c_{s63} = c_{s14} = c_{s24} = c_{s64} = c_{s15} = c_{s25} = c_{s65} \\ &= c_{s36} = c_{s46} = c_{s56} = 0 \end{aligned} \tag{22}$$

Therefore, by employing Eq. 1 and Eq. 6 to 22, the free-end compliance matrix C_S of any ICB can be obtained efficiently. In particular, straight beams can be regarded as a type of special ICBs with their curvature being 0 from its base to tip, the proposed method is logically applicable to straight beams as well.

3.3. Validation by Finite Element Analysis

In this section, we focus on verifying the proposed method in several different cases. In terms of the beam axis, Archimedean-spiral-curved beams and circular-curved beams are studied; regarding the shape of the cross-section, square, rectangular, round cross-sections and varying cross-section are analyzed in the following. In the end, the FEA results are presented to verify the analytical results.

3.3.1. *Geometric Definition of an Archimedean-spiral curved beam and a circular curved beam*

First, we need to geometrically define an Archimedean-spiral curved beam and a circular curved beam. The mathematical expression of Archimedean spirals in the polar coordinate system is written in Eq. 23:

$$r(\theta) = a + b\theta \tag{23}$$

where a and b are constant real numbers. a defines the distance between the centerpoint of the spiral and the origin

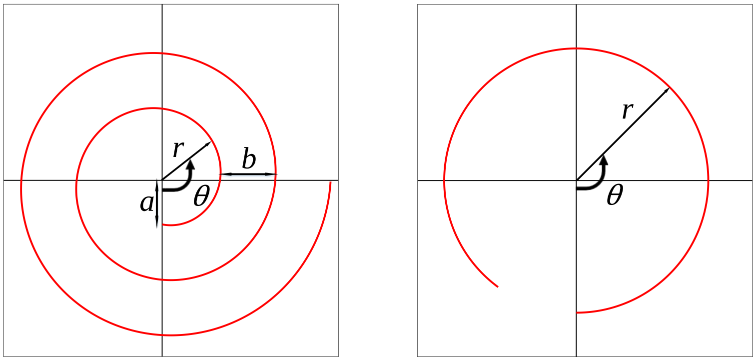

(a) Archimedean spiral

(b) Circular curve

Figure 5: Selected curves

while b controls the distance between loops and equivalently the growth rate of r shown in Fig. 5a. An Archimedean spiral is displayed in Fig. 5a, and it can be transformed to a circular curve displayed in Fig. 5b (right) when $b = 0$. The curvature K of Archimedean spirals can be defined [45]:

$$K(\theta) = \left| \frac{2(\frac{\mathrm{d}r}{\mathrm{d}\theta})^2 + r^2 - r\frac{\mathrm{d}^2 r}{\mathrm{d}\theta^2}}{(r^2 + (\frac{\mathrm{d}r}{\mathrm{d}\theta})^2)^{\frac{3}{2}}} \right| = \left| \frac{2b^2 + (a+b\theta)^2}{[(a+b\theta)^2 + b^2]^{\frac{3}{2}}} \right|$$

where K varies as θ changes. Logically, K can be simplified to a constant when it comes to circular curves ($b = 0$):

$$K = \frac{1}{a}$$

Therefore, an Archimedean-spiral curved beam (Fig. 6a) and a circular curved beam (Fig. 6c) are chosen to be studied as the representatives of varying-curvature curved beams and constant-curvature curved beams respectively.Their corresponding geometric expressions are noted in Eqs. 24 and 25:

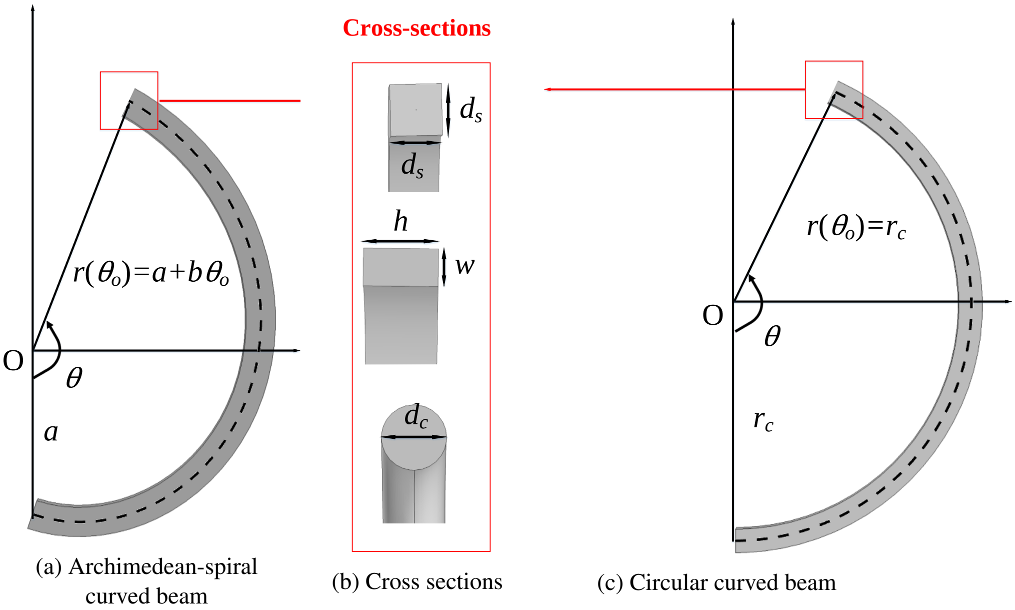

(a) Archimedean-spiral curved beam (b) Cross sections (c) Circular curved beam

Figure 6: Geometric definition of curved beams

Archimedean-spiral curved beam:

$$r(\theta) = a + b\theta, \theta \in [0, \theta_o] \tag{24}$$

Circular curved beam:

$$r(\theta) = r_c, \theta \in [0, \theta_o] \tag{25}$$

where the length unit and angular unit are m and rad respectively. The shape of the cross-section could be designed as the following three: square (with side length d_s), rectangular (with out-of-plane depth h and in-plane width w) and round (with diameter d_c) shown in Fig. 6b.

Apart from constant-cross-section beams like the ones in Fig. 6, the proposed method can also be used for analyzing varying-cross-section beams. As illustrated in Fig. 7, a circular varying-cross-section beam is defined: r_c is the radius of the circle; $h^*(\theta)$ and $w^*(\theta)$ are the varying cross-section parameters, which are dependent on θ. For verification purposes, an Archimedean-spiral curved beam with a constant square cross-section, a circular curved beam with a constant round cross-section and a circular curved beam with a uniformly varying rectangular cross-section are

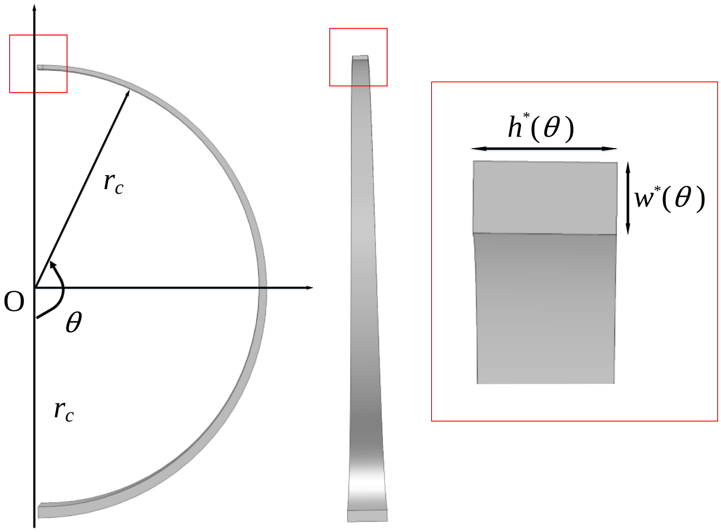

Figure 7: Geometric definition of varying-cross-section circular beams

chosen here with the dominant geometric parameters of the three studied beams assigned in (26)(27)(28):

The studied Archimedean-spiral curved beam with a constant square cross-section:

$$\begin{aligned}
&a = 0.030 \text{ m}\\
&b = 0.010 \text{ m}\\
&\theta_o = \pi\\
&d_s = 0.006 \text{ m}\\
&I_{m_z} = I_{m_{\hat{u}_n}} = \frac{d_s^4}{12} = 1.08 \times 10^{-10} \text{ m}^4\\
&I_p = d_s^4(\frac{1}{3} - 0.21\frac{d_s}{d_s}(1 - \frac{d_s^4}{12d_s^4})) = 1.83 \times 10^{-10} \text{ m}^4
\end{aligned} \tag{26}$$

The studied circular curved beam with a constant round cross-section:

$$\begin{aligned}
&r_c = 0.040 \text{ m}\\
&\theta_o = 0.75\pi\\
&d_c = 0.006 \text{ m}\\
&I_{m_z} = I_{m_{\hat{u}_n}} = \frac{\pi d_s^4}{64} = 6.36 \times 10^{-11} \text{ m}^4\\
&I_p = \frac{\pi d_s^4}{32} = 1.27 \times 10^{-10} \text{ m}^4
\end{aligned} \tag{27}$$

The studied circular curved beam with a uniformly varying rectangular cross-section:

$$\begin{aligned}
&r_c = 0.040 \text{ m}\\
&\theta_o = 0.5\pi\\
&h^*(\theta) = 0.007 \cdot (1 - 5r\theta) \text{ m}\\
&w^*(\theta) = 0.002 \cdot (1 - 5r\theta) \text{ m}\\
&I_{m_z} = \frac{h^*(\theta)w^*(\theta)^3}{12} \text{ m}^4\\
&I_{m_{\hat{u}_n}} = \frac{h^*(\theta)^3 w^*(\theta)}{12} \text{ m}^4\\
&I_p = h^*(\theta)w^*(\theta)^3(\frac{1}{3} - 0.21\frac{w^*(\theta)}{h^*(\theta)}(1 - \frac{w^*(\theta)^4}{12h^*(\theta)^4})) \text{ m}^4
\end{aligned} \tag{28}$$

It should be noticed that in (26)(28), the polar moment of inertia of the rectangular cross-section can be approximately described as Eq. 29 if $h \geq w$ [46][47]:

$$I_p = hw^3(\frac{1}{3} - 0.21\frac{w}{h}(1 - \frac{w^4}{12h^4})) \tag{29}$$

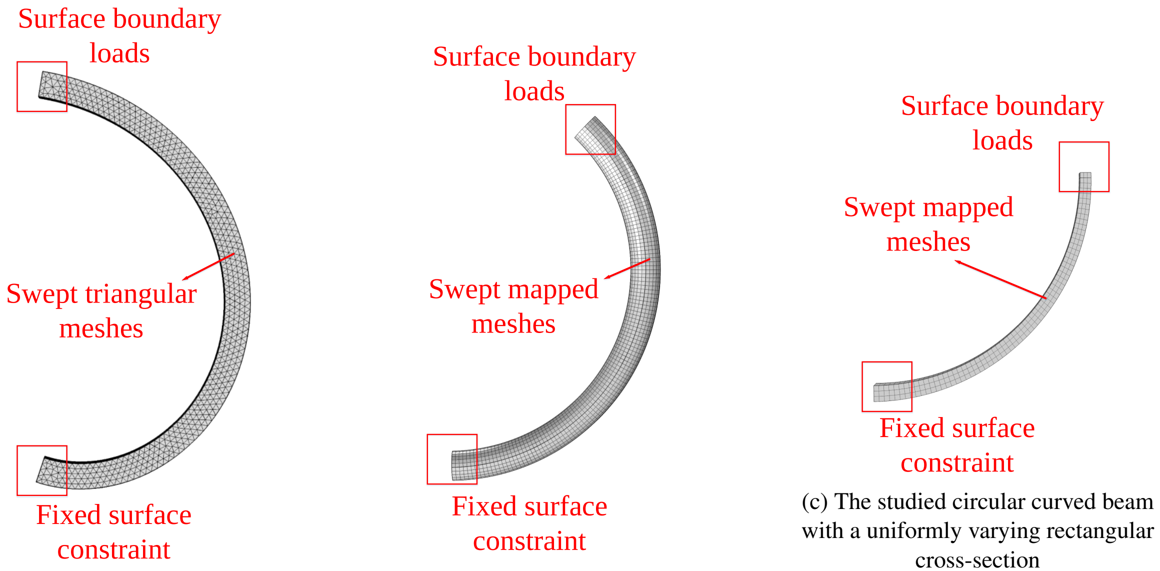

(a) The studied Archimedean-spiral curved beam with a constant square cross-section

(b) The studied circular curved beam with a constant round cross-section

(c) The studied circular curved beam with a uniformly varying rectangular cross-section

Figure 8: FEA boundary conditions

3.3.2. *Finite Element Analysis Compared with Analytical Results*

To validate the analytical compliance matrices of three beams defined in (26), (27) and (28), three FEA models are built in COMSOL. Swept triangular meshes and swept mapped meshes are used with the maximum and minimal mesh sizes being 0.02 mm and 2 mm respectively shown in Fig.8. The relative tolerance of the convergence error is set as 0.001 by default. The material used is isotropic structural steel with Young's modulus $E = 200 \times 10^9$ Pa and Poisson's ratio $\upsilon = 0.3$. Logically, the shear modulus G is calculated by $G = \frac{E}{(2(1+\upsilon))} = 7.7 \times 10^{10}$ Pa. We compare the compliance results between the analytical models and the FEA models of the mentioned three curved beams with regard to reference point (the free end) where the boundary conditions set up in FEA are demonstrated in Fig. 8. As the studied compliance matrices only capture the properties of small deformation without considering material non-linearity and geometric non-linearity, the same conditions are set up in FEA as well. The results are displayed in Table. 1, 2 and 3 where the maximum error is below 3% (the error ER is defined as $\frac{|\text{FEA}-\text{AM}|}{\text{FEA}} \times 100\%$). In terms of total computational cost between AM and FEA, the corresponding efficiencies of them dramatically improve (see the corresponding computational time in Table. 1, 2 and 3). That clearly implies the analytical method of deriving free-end compliance matrices for any ICB is feasible and much more efficient for further mechanism synthesis and optimization.

Table 1
Comparison of free-end compliance of the beam defined in (26) between the analytical results (denoted by AM) and FEA results

Results	c_{s11} (10^{-6} m/N)	$c_{s21} = c_{s12}$ (10^{-5} m/N)	$c_{s61} = c_{s16}$ (10^{-4} m/N)	c_{s22} (10^{-5} m/N)	$c_{s62} = c_{s26}$ (10^{-4} m/N)	c_{s66} (10^{-3} m/N)
AM	7.4481	1.0101	2.0235	2.3722	3.3366	6.8114
FEA	7.4083	1.0048	2.0142	2.3672	3.3306	6.7968
ER	0.54%	0.53%	0.46%	0.21%	0.18%	0.21%
Results	c_{s33} (10^{-5} m/N)	$c_{s43} = c_{s34}$ (10^{-4} m/N)	$c_{s53} = c_{s35}$ (10^{-4} m/N)	c_{s44} (10^{-3} m/N)	$c_{s54} = c_{s45}$ (10^{-4} m/N)	c_{s55} (10^{-3} m/N)
AM	4.3370	−2.9877	−4.2257	8.6522	−2.0787	8.6383
FEA	4.3197	−2.9751	−4.2132	8.6317	−2.0849	8.6132
ER	0.40%	0.42%	0.42%	0.24%	0.24%	0.29%

Total computational time	AM	0.21 s	FEA	62.65 s

Table 2
Comparison of free-end compliance of the beam defined in (27) between the analytical results (denoted by AM) and FEA results

Results	c_{s11} (10^{-7} m/N)	$c_{s21} = c_{s12}$ (10^{-6} m/N)	$c_{s61} = c_{s16}$ (10^{-6} m/N)	c_{s22} (10^{-5} m/N)	$c_{s62} = c_{s26}$ (10^{-4} m/N)	c_{s66} (10^{-3} m/N)
AM	9.7578	−1.1098	5.1591	1.5631	2.9843	7.4074
FEA	9.9000	−1.1155	5.0684	1.5703	2.9980	7.4426
ER	0.14%	0.50%	1.97%	0.46%	0.46%	0.47%
Results	c_{s33} (10^{-5} m/N)	$c_{s43} = c_{s34}$ (10^{-5} m/N)	$c_{s53} = c_{s35}$ (10^{-4} m/N)	c_{s44} (10^{-3} m/N)	$c_{s54} = c_{s45}$ (10^{-4} m/N)	c_{s55} (10^{-3} m/N)
AM	1.9412	−3.8134	−3.4320	8.7543	2.3578	8.2827
FEA	1.9555	−3.8134	−3.4545	8.8002	2.3147	8.3373
ER	0.73%	0.00%	0.65%	0.52%	1.86%	0.65%

Total computational time	AM	0.19 s	FEA	40.00 s

Table 3
Comparison of free-end compliance of the beam defined in (28) between the analytical results (denoted by AM) and FEA results

Results	c_{s11} (10^{-5} m/N)	$c_{s21} = c_{s12}$ (10^{-5} m/N)	$c_{s61} = c_{s16}$ (10^{-4} m/N)	c_{s22} (10^{-5} m/N)	$c_{s62} = c_{s26}$ (10^{-3} m/N)	c_{s66} (10^{-2} m/N)
AM	1.0961	−1.6552	−5.0131	2.9169	1.0416	5.1846
FEA	1.0913	−1.6489	−4.9971	2.9094	1.0388	5.1613
ER	0.44%	0.38%	0.32%	0.25%	0.27%	0.45%
Results	c_{s33} (10^{-5} m/N)	$c_{s43} = c_{s34}$ (10^{-5} m/N)	$c_{s53} = c_{s35}$ (10^{-4} m/N)	c_{s44} (10^{-2} m/N)	$c_{s54} = c_{s45}$ (10^{-2} m/N)	c_{s55} (10^{-2} m/N)
AM	1.7651	−3.3269	−5.4880	3.6384	1.0930	2.5657
FEA	1.7301	−3.2373	−5.3765	3.5511	1.0832	2.5304
ER	2.02%	2.77%	2.07%	2.46%	0.90%	1.40%

Total computational time	AM	0.23 s	FEA	15 s

4. Compliance Analysis and Mobility Optimization of Generic Planar Parallelogram and Ortho-planar Spring Integrating Initially Curved Beams

In this section, we aim to conduct planar compliance analysis of the generic ICB-based parallelogram and spatial compliance analysis of Ortho-planar spring both employing screw theory as a linear modeling method and using a normalization-based method [21] for comparison purposes, followed by mobility optimization of these mechanisms.

Recalling the concept of position-space-based reconfiguration method (PSR [4]), the layout of a compliant mechanism can be restructured via changing the positions of each independent compliant modules (ICMs [4]) within their permitted position ranges to design and optimize mobility, such as designing degrees of freedom (DOF) and degrees of constraints (DOC) or reducing their parasitic motions for more accurate translational and rotational movements. Essentially, by introducing positional parameters into compliance synthesis of CMs, the final compliance matrix of CMs can be expressed as functions of these introduced positional parameters, based on which the whole process can be transformed into an optimization problem. Apart from positional parameters, a representative geometric parameter of ICMs is included to be studied here, which is θ_o (defined in Fig. 1) of ICBs, providing more possibilities for mechanism performance.

Many decent studies about designing and optimizing the geometry of CMs tend to use enumeration graphing method to capture the trend of mechanism performance versus geometric parameters [15][32][48][49][50][51] for engineering aiding design. However, this method would have some limitations in the following scenarios. Firstly and most importantly, the enumeration graphing method would not be able to efficiently deal with multi-variable optimization problems especially when above three variables are studied. Secondly, multi-objective optimization problems are tough in this case if the objectives are conflicting, and decisions are normally made by designers' intuition and experience from enumeration graphs. Thirdly, in terms of single-objective optimization problem, it would be hard to ensure the global optimized solution when the trend is not monotonic [15][49][51]. For example, points of inflection may be excluded from enumerated ranges; improper sampling density may ignore the existence of points of inflection, resulting in wrong judgment about the trend. Last, it tends to be computationally expensive when obtaining enumerated numerical solutions [15]. To solve the mentioned problems, under the structure of Weighted-Sum Method [44], we use generic algorithm (or any gradient-based optimization algorithm) instead to directly obtain the globally optimized geometric parameters under the given multi-objectives, which is more efficient and straightforward.

Using the concept of PSR (but not being limited to PSR structure) and our optimization strategy, we'll be able to find out the globally optimized solutions of ICB-based mechanism synthesis for the given design requirements. Practical constraints (such as mechanical interference or dimensional limit) are considered as well in this optimization process. In consideration of easier manufacturing process and the promotion of standard parts, circular curved beams are chosen to be studied for the following mechanism synthesis and optimization.

4.1. Planar Compliance Analysis and Geometric Optimization of Parallelogram Mechanisms

4.1.1. Planar Compliance Modeling

Similar to the generic straight-beam-based parallelogram [41][51][52][53][54], the circular-curved-beam-based one is structured in a symmetric manner where the parallelogram is composed of a rigid base, a rigid motion stage and two legs in between the former two shown in Fig. 10. The legs are named as Leg 1 and Leg 2 where each leg comprises two compliant circular beams (labeled 11#, 12#, 21# and 22#) and one rigid link in between them. Logically, the general planar free-end compliance matrix $\boldsymbol{C_P}$ of ICBs can be deduced from the spatial compliance matrix $\boldsymbol{C_S}$ (defined in Eq. 2) into a 3-by-3 matrix:

$$\boldsymbol{C_P} = \begin{bmatrix} c_{p11} & c_{p12} & c_{p13} \\ c_{p21} & c_{p22} & c_{p23} \\ c_{p31} & c_{p32} & c_{p33} \end{bmatrix} = \begin{bmatrix} c_{s11} & c_{s12} & c_{s16} \\ c_{s21} & c_{s22} & c_{s26} \\ c_{s61} & c_{s62} & c_{s66} \end{bmatrix}$$

According to the proposed method (Eq. 9 to 14), the general planar free-end compliance matrix $\boldsymbol{C_{PC}}$ of circular-curved beams is formulated in Eq. 30:

$$\boldsymbol{C_{PC}} = \begin{bmatrix} c_{pc11} & c_{pc12} & c_{pc13} \\ c_{pc21} & c_{pc22} & c_{pc23} \\ c_{pc31} & c_{pc32} & c_{pc33} \end{bmatrix} \tag{30}$$

where

$$
\begin{aligned}
c_{pc11} &= \frac{r^3}{EI_{m_z}}\int_0^{\theta_o}(\sin(\theta_o)-\sin(\theta))^2\mathrm{d}\theta + \frac{r}{EA}\int_0^{\theta_o}(\sin(\theta))^2\mathrm{d}\theta;\\
c_{pc21} &= c_{pc12} = \pm[-(\frac{r^3}{EI_{m_z}}\int_0^{\theta_o}(\sin(\theta_o)-\sin(\theta))(\cos(\theta)-\cos(\theta_o))\mathrm{d}\theta - \frac{r}{EA}\int_0^{\theta_o}\sin(\theta)\cos(\theta)\mathrm{d}\theta)];\\
c_{pc31} &= c_{pc13} = \pm[-\frac{r^2}{EI_{m_z}}\int_0^{\theta_o}(\sin(\theta_o)-\sin(\theta))\mathrm{d}\theta];\\
c_{pc22} &= \frac{r^3}{EI_{m_z}}\int_0^{\theta_o}(\cos(\theta)-\cos(\theta_o))^2\mathrm{d}\theta + \frac{r}{EA}\int_0^{\theta_o}(\cos(\theta))^2\mathrm{d}\theta;\\
c_{pc32} &= c_{pc23} = \frac{r^2}{EI_{m_z}}\int_0^{\theta_o}(\cos(\theta)-\cos(\theta_o))\mathrm{d}\theta;\\
c_{pc33} &= \frac{r\theta_o}{EI_{m_z}}.
\end{aligned}
$$

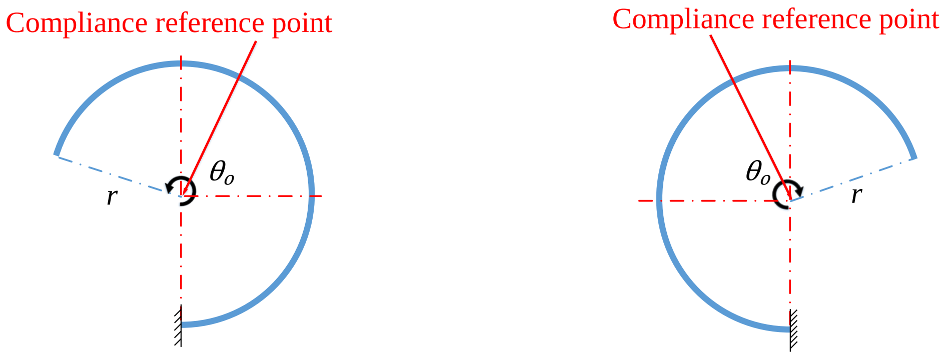

(a) Anti-clockwise circular-curved beam

(b) Clockwise circular-curved beam

Figure 9: Elementary flexible member: circular-curved beams

It's worth noticing that the choice of signs in c_{pc21}, c_{pc12}, c_{pc31} and c_{pc13} depends on the direction of beam axis from the base to the tip. If it's anti-clockwise like the beam shown in Fig. 9a, the sign is positive. Otherwise, it's negative (Fig. 9b). In the following paper, the compliance matrix of anti-clockwise ones are denoted as C_S, C_P and so on whereas the clockwise ones are denoted by C_S^* or C_P^*, etc for simplicity. For more convenient compliance synthesis, circular-curved beams need to be considered as a compliant kinematic hinge with its compliance reference point set up at the center of the circle displayed in Fig. 9. Therefore, the transferred compliance matrices C_{PC_c} from the free-end ones are derived in Eq. 31:

$$
\begin{aligned}
C_{PC_c} &= (D_{tr}^T(C_{PC})^{-1}D_{tr})^{-1}\\
C_{PC_c}^* &= (D_{tr}^{*T}(C_{PC}^*)^{-1}D_{tr}^*)^{-1}
\end{aligned}
\tag{31}
$$

where

$$
D_{tr} = \begin{bmatrix} 1 & 0 & -r\cos(\theta_o-\frac{\pi}{2}) \\ 0 & 1 & r\sin(\theta_o-\frac{\pi}{2}) \\ 0 & 0 & 1 \end{bmatrix}, \quad D_{tr}^* = \begin{bmatrix} 1 & 0 & r\cos(\theta_o-\frac{\pi}{2}) \\ 0 & 1 & r\sin(\theta_o-\frac{\pi}{2}) \\ 0 & 0 & 1 \end{bmatrix}
$$

As displayed in Fig. 10, the rotational position space of the circular-curved beam can be demonstrated by a dash-line circle with its center also at the compliance reference point where the exact rotational position can be defined by two

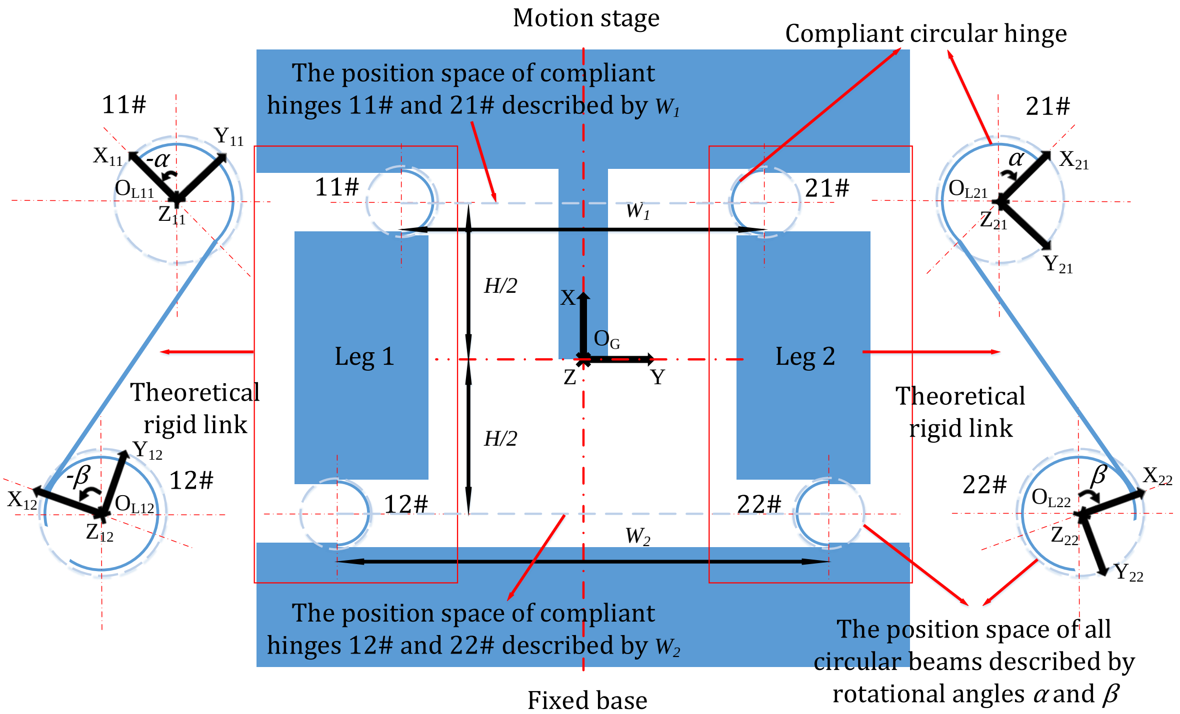

Figure 10: Schematic diagram of circular-beam-based planar mechanism

angles α and β ($-\alpha$ and $-\beta$ are used to locate beam 11# and beam 12# while α and β are used to locate beam 21# and beam 22#). The distance between the compliance reference points of beams 11# and 21# is denoted by W_1 while the distance between those of beams 12# and 22# is denoted by W_2, and they both describe the horizontal position space of the corresponding two beams. Besides, the distance between beams 11# and 12# or beams 21# and 22# is denoted by H, which is the characteristic length of the mechanism. also representing the overall dimension of the mechanism. The fixed global coordinate system $\mathrm{O_G - XYZ}$ is set up at a point which coincides with the geometric center of the undeformed mechanism and 4 local coordinate systems ($\mathrm{O_{L11} - X_{11}Y_{11}Z_{11}}$, $\mathrm{O_{L12} - X_{12}Y_{12}Z_{12}}$, $\mathrm{O_{L21} - X_{21}Y_{21}Z_{21}}$ and $\mathrm{O_{L22} - X_{22}Y_{22}Z_{22}}$) are defined at the 4 compliance reference points of the 4 circular beams respectively, which are all demonstrated in Fig. 10. With the predefined geometric parameters above, we can derive the planar compliance matrix of the whole mechanism C_{PG} at $\mathrm{O_G}$, starting from synthesizing the compliance matrix of every single compliant module (which are C_{L11} at $\mathrm{O_{L11}}$, C_{L12} at $\mathrm{O_{L12}}$, C_{L21} at $\mathrm{O_{L21}}$ and C_{L22} at $\mathrm{O_{L22}}$) using screw theory (Eq. 32):

$$C_{PG} = (((T_{11}^T D_{11}^T (R_{11} C_{L11} R_{11}^T)^{-1} D_{11} T_{11})^{-1} + (T_{12}^T D_{12}^T (R_{12} C_{L12} R_{12}^T)^{-1} D_{12} T_{12})^{-1})^{-1} + ((T_{21}^T D_{21}^T (R_{21} C_{L21} R_{21}^T)^{-1} D_{21} T_{21})^{-1} + (T_{22}^T D_{22}^T (R_{22} C_{L22} R_{22}^T)^{-1} D_{22} T_{22})^{-1})^{-1})^{-1} \tag{32}$$

where

$$R_{11} = \begin{bmatrix} \cos(-\alpha) & -\sin(-\alpha) & 0 \\ \sin(-\alpha) & \cos(-\alpha) & 0 \\ 0 & 0 & 1 \end{bmatrix}, D_{11} = \begin{bmatrix} 1 & 0 & 0 \\ 0 & 1 & H/2 \\ 0 & 0 & 1 \end{bmatrix}, T_{11} = \begin{bmatrix} 1 & 0 & W_1/2 \\ 0 & 1 & 0 \\ 0 & 0 & 1 \end{bmatrix};$$

$$R_{12} = \begin{bmatrix} \cos(-\beta) & -\sin(-\beta) & 0 \\ \sin(-\beta) & \cos(-\beta) & 0 \\ 0 & 0 & 1 \end{bmatrix}, D_{12} = \begin{bmatrix} 1 & 0 & 0 \\ 0 & 1 & -H/2 \\ 0 & 0 & 1 \end{bmatrix}, T_{12} = \begin{bmatrix} 1 & 0 & W_2/2 \\ 0 & 1 & 0 \\ 0 & 0 & 1 \end{bmatrix};$$

$$R_{21}=\begin{bmatrix}\cos(\alpha) & -\sin(\alpha) & 0\\ \sin(\alpha) & \cos(\alpha) & 0\\ 0 & 0 & 1\end{bmatrix},\ D_{21}=\begin{bmatrix}1 & 0 & 0\\ 0 & 1 & H/2\\ 0 & 0 & 1\end{bmatrix},\ T_{21}=\begin{bmatrix}1 & 0 & -W_1/2\\ 0 & 1 & 0\\ 0 & 0 & 1\end{bmatrix};$$

$$R_{22}=\begin{bmatrix}\cos(\beta) & -\sin(\beta) & 0\\ \sin(\beta) & \cos(\beta) & 0\\ 0 & 0 & 1\end{bmatrix},\ D_{22}=\begin{bmatrix}1 & 0 & 0\\ 0 & 1 & -H/2\\ 0 & 0 & 1\end{bmatrix},\ T_{22}=\begin{bmatrix}1 & 0 & -W_2/2\\ 0 & 1 & 0\\ 0 & 0 & 1\end{bmatrix}.$$

In particular, the different choices of anti-clockwise beams and clockwise beam as the elementary flexible members in the mechanism synthesis result in four combinations/scenarios:

- Scenario A

  $$C_{L11}=C_{L12}=C_{PC_c}$$
  $$C_{L21}=C_{L22}=C^*_{PC_c}$$

- Scenario B

  $$C_{L11}=C_{L12}=C^*_{PC_c}$$
  $$C_{L21}=C_{L22}=C_{PC_c}$$

- Scenario C

  $$C_{L12}=C_{L21}=C_{PC_c}$$
  $$C_{L11}=C_{L22}=C^*_{PC_c}$$

- Scenario D

  $$C_{L12}=C_{L21}=C^*_{PC_c}$$
  $$C_{L11}=C_{L22}=C_{PC_c}$$

So far, we can obtain the final planar compliance matrix C_{PG} of the circular-beam-based parallelogram (Eq. 33):

$$C_{PG}=\begin{bmatrix}c_{pg11} & 0 & 0\\ 0 & c_{pg22} & c_{pg23}\\ 0 & c_{pg32} & c_{pg33}\end{bmatrix} \tag{33}$$

Its normalized compliance matrix C_{PG_n} can be formulated (see details in [21]) as follows for non-dimensional comparison (Eq. 34):

$$C_{PG_n}=\begin{bmatrix}c_{pg_n11} & 0 & 0\\ 0 & c_{pg_n22} & c_{pg_n23}\\ 0 & c_{pg_n32} & c_{pg_n33}\end{bmatrix}=\begin{bmatrix}\frac{c_{pg11}}{\frac{H^3}{EI_{m_z}}} & 0 & 0\\ 0 & \frac{c_{pg22}}{\frac{H^3}{EI_{m_z}}} & \frac{c_{pg23}}{\frac{H^2}{EI_{m_z}}}\\ 0 & \frac{c_{pg32}}{\frac{H^2}{EI_{m_z}}} & \frac{c_{pg33}}{\frac{H}{EI_{m_z}}}\end{bmatrix} \tag{34}$$

4.1.2. Geometric Optimization Strategy

Since α, β, W_1 and W_2 that describe the position spaces of all compliant hinges and one geometric parameter θ_o of circular curved beams are the key parameters to be studied for further mechanism optimization, the rest geometric and material parameters are assigned in (35):

$$\begin{aligned} &E = 69 \times 10^9 \text{ Pa} \\ &\upsilon = 0.3 \\ &w = 0.001 \text{ m} \\ &h = 0.003 \text{ m} \\ &r = 0.010 \text{ m} \\ &H = 0.080 \text{ m} \end{aligned} \tag{35}$$

Therefore, all elements in C_{PG_n} are the functions of the studied five parameters: α, β, W_1, W_2 and θ_o, depending on which the process of improving the performance of the mechanism is logically deduced into a multi-variable (α, β, W_1, W_2 and θ_o) and multi-objective (to maximize $\frac{c_{pg_n22}}{c_{pg_n11}}$, $\frac{c_{pg_n22}}{c_{pg_n33}}$ and $\frac{c_{pg_n22}}{c_{pg_n23}}$) optimization problem. c_{pg_n22} stands for the compliance in Y direction (primary motion) whereas c_{pg_n11} and c_{pg_n33} stands for the compliance in X and Z directions (undesired motions); c_{pg_n23} and c_{pg_n32} are the compliance of parasitic motion regarding Y and Z directions. Therefore, the three objectives $\frac{c_{pg_n22}}{c_{pg_n11}}$, $\frac{c_{pg_n22}}{c_{pg_n33}}$ and $\frac{c_{pg_n22}}{c_{pg_n23}}$ imply that by maximizing the ratio of primary-motion compliance to undesired-motion and parasitic compliance under given constraints, the optimal designs can be obtained accordingly. To deal with these multi objectives, Weighted-Sum Method [44] is used, which scalarizes a set of objectives into a single objective by pre-multiplying each objective with a user-supplied weight:

$$\begin{aligned} \max \quad & Z(\alpha, \beta, W_1, W_2, \theta_o) = \epsilon_1 \frac{c_{pg_n22}}{c_{pg_n11}} + \epsilon_2 \frac{c_{pg_n22}}{c_{pg_n33}} + \epsilon_3 \frac{c_{pg_n22}}{c_{pg_n23}} \\ s.t. \quad & -\pi \leq \alpha \leq \pi \\ & -\pi \leq \beta \leq \pi \\ & 2r + w < W_1 \leq H \\ & 2r + w < W_2 \leq H \\ & \pi/2 \leq \theta_o \leq 3\pi/2 \end{aligned} .$$

where ϵ_1, ϵ_2 and ϵ_3 are the weights of each single-optimized target respectively satisfying $\epsilon_1 + \epsilon_2 + \epsilon_3 = 1$; $Z(\alpha, \beta, W_1, W_2, \theta_o)$ is the objective function; Taking their importance into account, ϵ_1, ϵ_2 and ϵ_3 are assigned: $\epsilon_1 = \epsilon_2 = \epsilon_3 = 1/3$. The built-in Genetic Algorithm in MATLAB is used to obtain the globally optimal results with the following key parameters assigned: the population size is set up as 50; the number of maximum stall generations is assigned to 100; the random numbers generated within the bounds of the mentioned five variables are chosen as the initial population.

4.1.3. Globally Optimal Results with FEA Verification

The globally optimal results of Scenarios A, B, C and D are listed in (36), (37), (38) and (39) respectively with the corresponding consequent normalized compliance information obtained from the analytical models and FEA verification displayed in Tables. 4 to 7 and their geometric shapes illustrated in Figs. 11a to 11d. The optimal design of Scenario A (Fig. 11a) has two inverted legs whereas that of Scenario B (Fig. 11b) has two non-inverted legs. The optimal designs of Scenario C (Fig. 11c) and D (Fig. 11d) present hybrid structures of the former two, both having two half-inverted legs in them. According to Tables. 4 to 7, the analytical results are verified by FEA results with maximum error being 2.73%. The values of $\frac{c_{pg_n22}}{c_{pg_n11}}$ and $\frac{c_{pg_n22}}{c_{pg_n33}}$ are up to around 2000 and 700 respectively, which implies that the optimal mechanisms present DOF in Y direction and DOC in X direction and around Z axis. The ratio $\frac{c_{pg_n23}}{c_{pg_n22}}$ reaches 0, indicating that the mechanism nearly has no X-axis parasitic motion when translationally moving in Y direction. It should be remarked that the conclusions above are only valid when deformation is small.

In the FEA, the boundary conditions were set up in the same manner of the analytical models where the compliance reference point of whole mechanism C_{PG} at O_G (Fig. 10) was evaluated (Fig. 12): the motion stage and 2 thick links were set up as rigid bodies in COMSOL while the rest 4 compliant beams were set as deformable bodies (Fig. 12); swept mapped meshes were used with the maximum and minimal mesh sizes being 0.02 mm and 2 mm respectively; the relative tolerance of the convergence error was set as 0.001 by default; only small deformations were considered so geometric non-linearity function was not activated; the geometric and material parameters were chosen from (35), (36), (37), (38) and (39) respectively.

- * Globally Optimal Results of Scenario A

$$\alpha = -\frac{3\pi}{4};\ \beta = -\frac{3\pi}{4};\ W_1 = H = 0.080\ \text{m};\ W_2 = H = 0.080\ \text{m};\ \theta_o = \frac{\pi}{2} \tag{36}$$

- * Globally Optimal Results of Scenario B

$$\alpha = -\frac{\pi}{4};\ \beta = -\frac{\pi}{4};\ W_1 = H = 0.080\ \text{m};\ W_2 = H = 0.080\ \text{m};\ \theta_o = \frac{\pi}{2} \tag{37}$$

- * Globally Optimal Results of Scenario C

$$\alpha = -\frac{\pi}{4};\ \beta = -\frac{3\pi}{4};\ W_1 = H = 0.080\ \text{m};\ W_2 = H = 0.080\ \text{m};\ \theta_o = \frac{\pi}{2} \tag{38}$$

- * Globally Optimal Results of Scenario D

$$\alpha = -\frac{3\pi}{4};\ \beta = -\frac{\pi}{4};\ W_1 = H = 0.080\ \text{m};\ W_2 = H = 0.080\ \text{m};\ \theta_o = \frac{\pi}{2} \tag{39}$$

Table 4
Comparison between analytical results and FEA (without considering geometric non-linearity) results regarding the globally optimal design of Scenario A

Scenarios A	Results	c_{pg_n11}	c_{pg_n22}	c_{pg_n33}	$\frac{c_{pg_n22}}{c_{pg_n11}}$	$\frac{c_{pg_n22}}{c_{pg_n33}}$	$\frac{c_{pg_n23}}{c_{pg_n22}}$
$\alpha = -\frac{3\pi}{4}$ $\beta = -\frac{3\pi}{4}$ $\theta_o = \frac{\pi}{2}$ $W_1 = 0.080$ m $W_2 = 0.080$ m	AM	2.5839×10^{-5}	4.9645×10^{-2}	6.8843×10^{-5}	1.9213×10^{3}	7.2113×10^{2}	≈ 0
	FEA	2.6256×10^{-5}	4.9105×10^{-2}	6.9937×10^{-4}	1.8702×10^{3}	7.0213×10^{2}	≈ 0
	ER	1.59%	1.10%	1.56%	2.73%	2.71%	≈ 0%

Table 5
Comparison between analytical results and FEA (without considering geometric non-linearity) results regarding the globally optimal design of Scenario B

Scenarios A	Results	c_{pg_n11}	c_{pg_n22}	c_{pg_n33}	$\frac{c_{pg_n22}}{c_{pg_n11}}$	$\frac{c_{pg_n22}}{c_{pg_n33}}$	$\frac{c_{pg_n23}}{c_{pg_n22}}$
$\alpha = -\frac{\pi}{4}$ $\beta = -\frac{\pi}{4}$ $\theta_o = \frac{\pi}{2}$ $W_1 = 0.080$ m $W_2 = 0.080$ m	AM	2.5839×10^{-5}	4.9645×10^{-2}	6.8843×10^{-5}	1.9213×10^{3}	7.2113×10^{2}	≈ 0
	FEA	2.6256×10^{-5}	4.9105×10^{-2}	6.9937×10^{-4}	1.8702×10^{3}	7.0213×10^{2}	≈ 0
	ER	1.59%	1.10%	1.56%	2.73%	2.71%	≈ 0%

Table 6
Comparison between analytical results and FEA (without considering geometric non-linearity) results regarding the globally optimal design of Scenario C

Scenarios A	Results	c_{pg_n11}	c_{pg_n22}	c_{pg_n33}	$\frac{c_{pg_n22}}{c_{pg_n11}}$	$\frac{c_{pg_n22}}{c_{pg_n33}}$	$\frac{c_{pg_n23}}{c_{pg_n22}}$
$\alpha = -\frac{\pi}{4}$ $\beta = -\frac{3\pi}{4}$ $\theta_o = \frac{\pi}{2}$ $W_1 = 0.080$ m $W_2 = 0.080$ m	AM	2.5839×10^{-5}	4.9645×10^{-2}	6.8843×10^{-5}	1.9213×10^{3}	7.2113×10^{2}	≈ 0
	FEA	2.6256×10^{-5}	4.9105×10^{-2}	6.9937×10^{-4}	1.8702×10^{3}	7.0213×10^{2}	≈ 0
	ER	1.59%	1.10%	1.56%	2.73%	2.71%	≈ 0%

Table 7
Comparison between analytical results and FEA (without considering geometric non-linearity) results regarding the globally optimal design of Scenario D

Scenarios A	Results	$c_{pg_n 11}$	$c_{pg_n 22}$	$c_{pg_n 33}$	$\frac{c_{pg_n 22}}{c_{pg_n 11}}$	$\frac{c_{pg_n 22}}{c_{pg_n 33}}$	$\frac{c_{pg_n 23}}{c_{pg_n 22}}$
$\alpha = -\frac{3\pi}{4}$ $\beta = -\frac{\pi}{4}$ $\theta_o = \frac{\pi}{2}$ $W_1 = 0.080$ m $W_2 = 0.080$ m	AM	2.5839×10^{-5}	4.9645×10^{-2}	6.8843×10^{-5}	1.9213×10^{3}	7.2113×10^{2}	≈ 0
	FEA	2.6256×10^{-5}	4.9105×10^{-2}	6.9937×10^{-4}	1.8702×10^{3}	7.0213×10^{2}	≈ 0
	ER	1.59%	1.10%	1.56%	2.73%	2.71%	$\approx 0\%$

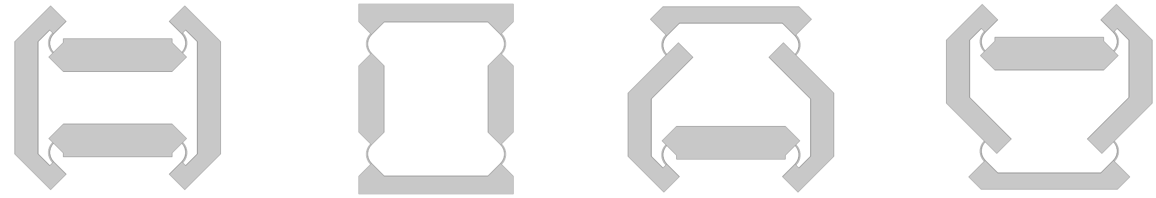
(a) The optimal design of Scenario A

(b) The optimal design of Scenario B

(c) The optimal design of Scenario C

(d) The optimal design of Scenario D

Figure 11: The optimal designs of circular-curved-beam-based parallelogram

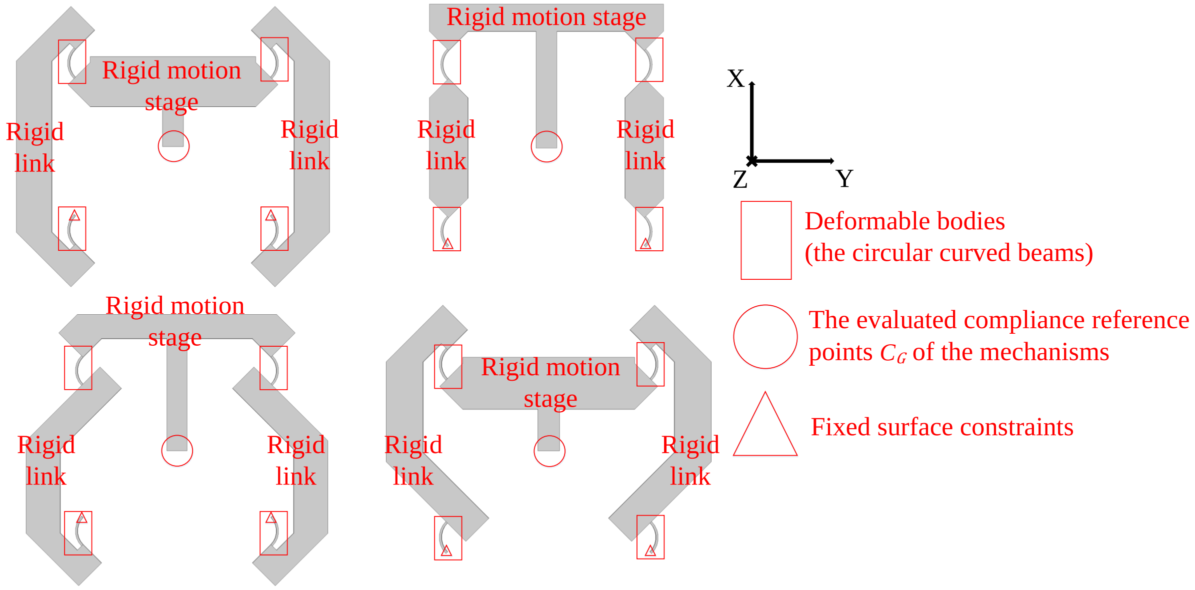

Figure 12: FEA verification boundary conditions of the optimal designs from Scenario A to D

4.1.4. *Design of Circular-curved-beam-based Parallelograms with Bidirectional Anti-buckling Capacity*

Similar to straight-beam-based parallelograms, load-bearing capacity is also one of the key performances of ICB-based parallelograms. Although the proposed optimal design from Scenario B (see Fig. 11b) does not experience mechanism buckling under heavy compression payloads, it still suffers from obvious stiffness reduction along payload direction (the negative X direction) illustrated in Fig. 13a where the relationship of X-axis stiffness against X-axis displacement was obtained from FEA with nonlinear geometry function activated and Y-axis displacement fixed to 0. It should be noticed that the X-axis stiffness gradually increases along the positive X axis, which implies the stiffness of the mechanism will increase if tension payloads are exerted. Due to the involvement of inverted legs in the optimal design from Scenario B (see Fig. 11a), a similar plot displaying an anti-symmetric relationship is illustrated in Fig. 13b. Inspired by their X-axis stiffness properties, a unique design that makes the most of the

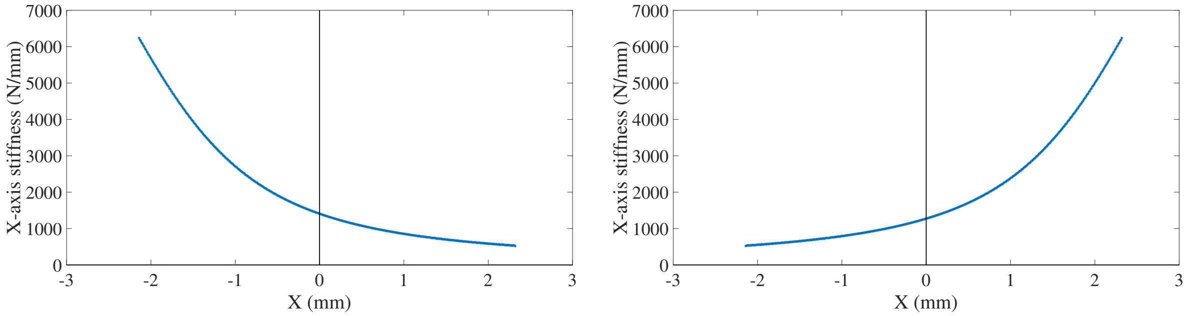

(a) The optimal design from Scenario A

(b) The optimal design from Scenario B

Figure 13: X-axis stiffness against X-axis displacement relationship of the optimal design from Scenario A and B

optimal designs of Scenario A (Fig. 11a) and Scenario B (Fig. 11b) was proposed (Fig. 14a), where no matter payloads in positive or negative X directions are exerted, there are always four circular-curved beams under tension and four under compression to compensate stiffness reduction in bidirections. In particular, W_a and W_b are introduced to define the horizontal distances of inverted legs and non-inverted legs respectively. Its relationship of X-axis stiffness against X-axis displacement obtained from FEA (where $W_a = 0.080$ m and $W_b = 0.010$ m with the rest geometric and material parameters and boundary conditions unchanged) is displayed Fig. 14b: the X-axis stiffness increases along both negative and positive X directions, which proves that the new design present bidirectional anti-buckling and high load-bearing capacity. Compared with the straight-beam-involved anti-buckling mechanism proposed in our previous work [15], this ICB-based design doesn't does experience stiffness reduction under heavy payloads but the former does (see Fig. 16 in [15]), which presents better load-bearing ability.

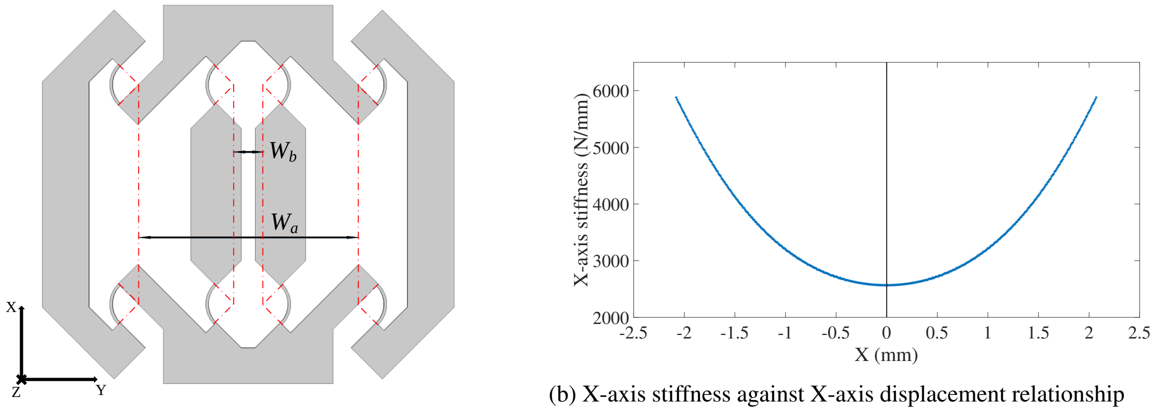

(a) The geometric shape of the proposed design that employs inverted and non-inverted legs

(b) X-axis stiffness against X-axis displacement relationship of the proposed design

Figure 14: The proposed design with high load-bearing and anti-buckling capacity

4.2. Spatial Compliance Analysis and Geometric Optimization of an circular-beam-based Ortho-planar Spring

As a classic type of compliant linear motion mechanisms, Ortho-planar springs have many advantages [34][55][56]: they're compact; they are located in a plane, but being able to provide non-rotating out-of-plane translational motion; they can be easily manufactured in a single piece of material; it has the potential for larger deflections than conventional planar springs. From a mechanical point of view, Ortho-planar springs are composed of a base, a central motion platform and several U-shaped legs (Fig.15) where each leg is divided into two thin flexible beams [34]. Ortho-planar springs are commonly used in many applications especially sophisticated and compact mechanisms: sensors [57][58][59]; one-way micro-valve that can be used in a micro-pump [56]; microelectromechanical systems [60];

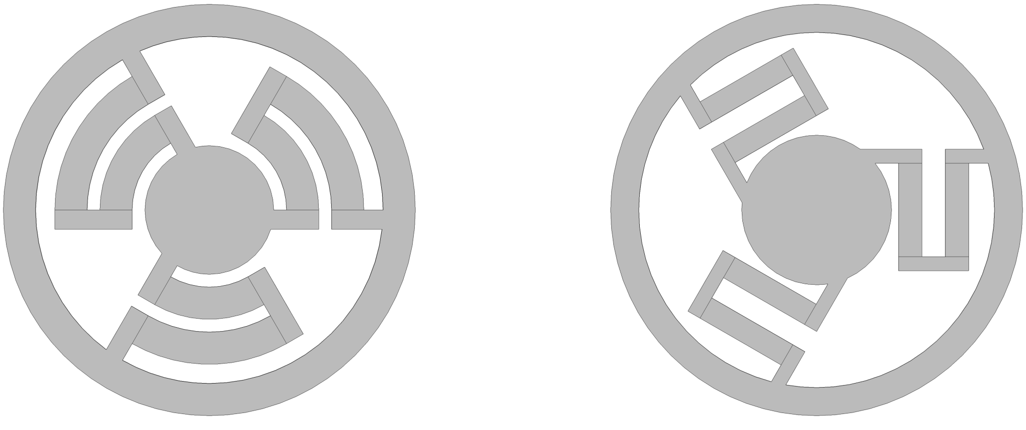

(a) Circular-curved-beam-based Ortho-planar Spring (b) Straight-beam-based Ortho-planar Spring

Figure 15: Ortho-planar Springs

continuum robots [49][61][62][63]. Fig.15 demonstrates two types of Ortho-planar springs: circular-beam-based ones (Fig. 15a) and straight-beam-based ones (Fig. 15b) where [49][61][62][63] have conducted spatial compliance analysis of the straight-beam-based Ortho-planar springs. In this section, we aim to conduct spatial compliance analysis of circular-beam-based ones, followed by geometric optimization via genetic algorithm. FEA validation is presented to verify the optimal analytical results.

4.2.1. Spatial Compliance Modeling

In this section, we aim to conduct spatial compliance analysis of circular-curved-beam-based Ortho-planar springs where the derivation of compliance matrix of a single circular curved beam C_{SC} is first presented via the proposed method (Eqs. 6 to 22 and Eq. 25) shown in Eq. 40:

$$C_{SC} = \begin{bmatrix} c_{sc11} & c_{sc12} & 0 & 0 & 0 & c_{sc16} \\ c_{sc21} & c_{sc22} & 0 & 0 & 0 & c_{sc26} \\ 0 & 0 & c_{sc33} & c_{sc34} & c_{sc35} & 0 \\ 0 & 0 & c_{sc43} & c_{sc44} & c_{sc45} & 0 \\ 0 & 0 & c_{sc53} & c_{sc54} & c_{sc55} & 0 \\ c_{sc61} & c_{sc62} & 0 & 0 & 0 & c_{sc66} \end{bmatrix} \tag{40}$$

where

$$c_{sc11} = \frac{r^3}{EI_{m_z}} \int_0^{\theta_o} (\sin(\theta_o) - \sin(\theta))^2 \mathrm{d}\theta + \frac{r}{EA} \int_0^{\theta_o} (\sin(\theta))^2 \mathrm{d}\theta;$$

$$c_{sc21} = c_{sc12} = -\left(\frac{r^3}{EI_{m_z}} \int_0^{\theta_o} (\sin(\theta_o) - \sin(\theta))(\cos(\theta) - \cos(\theta_o)) \mathrm{d}\theta - \frac{r}{EA} \int_0^{\theta_o} \sin(\theta)\cos(\theta) \mathrm{d}\theta\right);$$

$$c_{sc61} = c_{sc16} = -\frac{r^2}{EI_{m_z}} \int_0^{\theta_o} (\sin(\theta_o) - \sin(\theta)) \mathrm{d}\theta;$$

$$c_{sc22} = \frac{r^3}{EI_{m_z}} \int_0^{\theta_o} (\cos(\theta) - \cos(\theta_o))^2 \mathrm{d}\theta + \frac{r}{EA} \int_0^{\theta_o} (\cos(\theta))^2 \mathrm{d}\theta;$$

$$c_{sc62} = c_{sc26} = \frac{r^2}{EI_{m_z}} \int_0^{\theta_o} (\cos(\theta) - \cos(\theta_o)) \mathrm{d}\theta;$$

$$c_{sc66} = \frac{r\theta_o}{EI_{m_z}}.$$

$$c_{sc33}=\frac{r^3}{EI_{m_{\hat{u}_n}}}\int_0^{\theta_o}(\sin(\pi-\theta_o+\theta))^2\mathrm{d}\theta+\frac{r^3}{GI_p}\int_0^{\theta_o}(1+\cos(\pi-\theta_o+\theta))^2\mathrm{d}\theta;$$

$$c_{sc62}=c_{sc26}=\frac{r^2}{EI_{m_z}}\int_0^{\theta_o}(\cos(\theta)-\cos(\theta_o))\mathrm{d}\theta;$$

$$c_{sc66}=\frac{r\theta_o}{EI_{m_z}}.$$

$$c_{sc33}=\frac{r^3}{EI_{m_{\hat{u}_n}}}\int_0^{\theta_o}(\sin(\pi-\theta_o+\theta))^2\mathrm{d}\theta+\frac{r^3}{GI_p}\int_0^{\theta_o}(1+\cos(\pi-\theta_o+\theta))^2\mathrm{d}\theta;$$

$$c_{sc53}=c_{sc35}=-\frac{r^2}{EI_{m_{\hat{u}_n}}}\int_0^{\theta_o}\sin(\pi-\theta_o+\theta)\sin(\theta)\mathrm{d}\theta-\frac{r^2}{GI_p}\int_0^{\theta_o}(1+\cos(\pi-\theta_o+\theta))\cos(\theta)\mathrm{d}\theta;$$

$$c_{sc44}=\frac{r}{EI_{m_{\hat{u}_n}}}\int_0^{\theta_o}(\cos(\theta))^2\mathrm{d}\theta+\frac{r}{GI_p}\int_0^{\theta_o}(\sin(\theta))^2\mathrm{d}\theta;$$

$$c_{sc54}=c_{sc45}=-\frac{r}{EI_{m_{\hat{u}_n}}}\int_0^{\theta_o}\cos(\theta)\sin(\theta)\mathrm{d}\theta+\frac{r}{GI_p}\int_0^{\theta_o}\cos(\theta)\sin(\theta)\mathrm{d}\theta;$$

$$c_{sc55}=\frac{r}{EI_{m_{\hat{u}_n}}}\int_0^{\theta_o}(\sin(\theta))^2\mathrm{d}\theta+\frac{r}{GI_p}\int_0^{\theta_o}(\cos(\theta))^2\mathrm{d}\theta;$$

Similarly, we can obtain the spatial compliance matrix C_{SG} at O_G on the motion stage of the Ortho-planar spring from every single flexible member (Fig. 16) shown in Eq. 41:

$$\begin{aligned}C_{SG}=&(D_3^T((D_2(R_2(D_1^T(R_1C_{SC_2}R_1^T)^{-1}D_1)^{-1}R_2^T)^{-1}D_2)^{-1}+R_4R_3C_{SC_1}R_3^TR_4^T)^{-1}D_3\\&+R_5D_3^T((D_2(R_2(D_1^T(R_1C_{SC_2}R_1^T)^{-1}D_1)^{-1}R_2^T)^{-1}D_2)^{-1}+R_4R_3C_{SC_1}R_3^TR_4^T)^{-1}D_3R_5^T\\&+R_6D_3^T((D_2(R_2(D_1^T(R_1C_{SC_2}R_1^T)^{-1}D_1)^{-1}R_2^T)^{-1}D_2)^{-1}+R_4R_3C_{SC_1}R_3^TR_4^T)^{-1}D_3R_6^T)^{-1}\end{aligned}\tag{41}$$

where

$$R_1=\begin{bmatrix}\cos(\theta_o-\frac{\pi}{2}) & -\sin(\theta_o-\frac{\pi}{2}) & 0 & 0 & 0 & 0\\ \sin(\theta_o-\frac{\pi}{2}) & \cos(\theta_o-\frac{\pi}{2}) & 0 & 0 & 0 & 0\\ 0 & 0 & 1 & 0 & 0 & 0\\ 0 & 0 & 0 & \cos(\theta_o-\frac{\pi}{2}) & -\sin(\theta_o-\frac{\pi}{2}) & 0\\ 0 & 0 & 0 & \sin(\theta_o-\frac{\pi}{2}) & \cos(\theta_o-\frac{\pi}{2}) & 0\\ 0 & 0 & 0 & 0 & 0 & 1\end{bmatrix};$$

$$R_2=\begin{bmatrix}\cos(\pi) & -\sin(\pi) & 0 & 0 & 0 & 0\\ \sin(\pi) & \cos(\pi) & 0 & 0 & 0 & 0\\ 0 & 0 & 1 & 0 & 0 & 0\\ 0 & 0 & 0 & \cos(\pi) & -\sin(\pi) & 0\\ 0 & 0 & 0 & \sin(\pi) & \cos(\pi) & 0\\ 0 & 0 & 0 & 0 & 0 & 1\end{bmatrix};\ R_3=\begin{bmatrix}1 & 0 & 0 & 0 & 0 & 0\\ 0 & \cos(\pi) & -\sin(\pi) & 0 & 0 & 0\\ 0 & \sin(\pi) & \cos(\pi) & 0 & 0 & 0\\ 0 & 0 & 0 & 1 & 0 & 0\\ 0 & 0 & 0 & 0 & \cos(\pi) & -\sin(\pi)\\ 0 & 0 & 0 & 0 & \sin(\pi) & \cos(\pi)\end{bmatrix};$$

$$R_4=\begin{bmatrix}\cos(\frac{\pi}{2}) & -\sin(\frac{\pi}{2}) & 0 & 0 & 0 & 0\\ sin(\frac{\pi}{2}) & \cos(\frac{\pi}{2}) & 0 & 0 & 0 & 0\\ 0 & 0 & 1 & 0 & 0 & 0\\ 0 & 0 & 0 & 1 & 0 & 0\\ 0 & 0 & 0 & 0 & \cos(\frac{\pi}{2}) & -\sin(\frac{\pi}{2})\\ 0 & 0 & 0 & 0 & \sin(\frac{\pi}{2}) & \cos(\frac{\pi}{2})\end{bmatrix};\ R_5=\begin{bmatrix}\cos(-\frac{2\pi}{3}) & -\sin(-\frac{2\pi}{3}) & 0 & 0 & 0 & 0\\ sin(-\frac{2\pi}{3}) & \cos(-\frac{2\pi}{3}) & 0 & 0 & 0 & 0\\ 0 & 0 & 1 & 0 & 0 & 0\\ 0 & 0 & 0 & \cos(-\frac{2\pi}{3}) & -\sin(-\frac{2\pi}{3}) & 0\\ 0 & 0 & 0 & \sin(-\frac{2\pi}{3}) & \cos(-\frac{2\pi}{3}) & 0\\ 0 & 0 & 0 & 0 & 0 & 1\end{bmatrix}$$

;

$$R_6 = \begin{bmatrix} \cos(-\frac{4\pi}{3}) & -\sin(-\frac{4\pi}{3}) & 0 & 0 & 0 & 0 \\ sin(-\frac{4\pi}{3}) & \cos(-\frac{4\pi}{3}) & 0 & 0 & 0 & 0 \\ 0 & 0 & 1 & 0 & 0 & 0 \\ 0 & 0 & 0 & \cos(-\frac{4\pi}{3}) & -\sin(-\frac{4\pi}{3}) & 0 \\ 0 & 0 & 0 & \sin(-\frac{4\pi}{3}) & \cos(-\frac{4\pi}{3}) & 0 \\ 0 & 0 & 0 & 0 & 0 & 1 \end{bmatrix};$$

$$D_1 = \begin{bmatrix} 1 & 0 & 0 & 0 & 0 & -d \\ 0 & 1 & 0 & 0 & 0 & 0 \\ 0 & 0 & 1 & d & 0 & 0 \\ 0 & 0 & 0 & 1 & 0 & 0 \\ 0 & 0 & 0 & 0 & 1 & 0 \\ 0 & 0 & 0 & 0 & 0 & 1 \end{bmatrix}; D_2 = \begin{bmatrix} 1 & 0 & 0 & 0 & 0 & -r_1(-1+\cos(\theta_o)) \\ 0 & 1 & 0 & 0 & 0 & -r_1\sin(\theta_o) \\ 0 & 0 & 1 & r_1(-1+\cos(\theta_o)) & r_1\sin(\theta_o) & 0 \\ 0 & 0 & 0 & 1 & 0 & 0 \\ 0 & 0 & 0 & 0 & 1 & 0 \\ 0 & 0 & 0 & 0 & 0 & 1 \end{bmatrix};$$

$$D_3 = \begin{bmatrix} 1 & 0 & 0 & 0 & 0 & r_1\cos(\theta_o) \\ 0 & 1 & 0 & 0 & 0 & r_1\sin(\theta_o) \\ 0 & 0 & 1 & -r_1\cos(\theta_o) & -r_1\sin(\theta_o) & \\ 0 & 0 & 0 & 1 & 0 & 0 \\ 0 & 0 & 0 & 0 & 1 & 0 \\ 0 & 0 & 0 & 0 & 0 & 1 \end{bmatrix};$$ C_{SC_1} and C_{SC_2}, which can be derived according to Eq. 40, stand for the compliance matrices of circular-curved beams 1# ($r = r_1$) and 2# ($r = r_1 + d$) shown in Fig. 16.

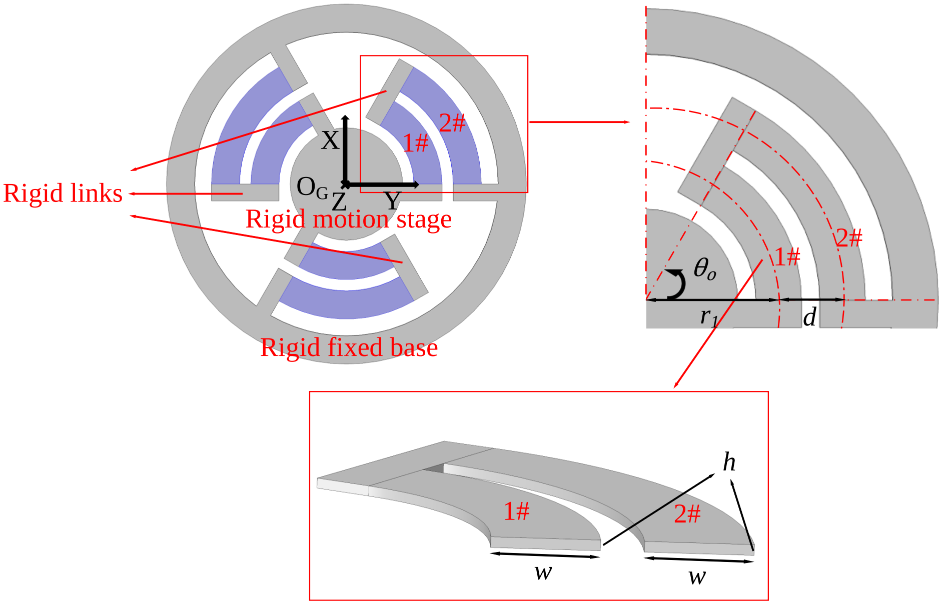

Figure 16: Detailed geometric information of curved-beam-based Ortho-planar springs

Then, we finally arrive at the symbolic spatial compliance matrix C_{SG} of the Ortho-planar springs, which is structured in a diagonal manner (Eq. 42):

$$C_{SG} = \begin{bmatrix} c_{sg11} & 0 & 0 & 0 & 0 & 0 \\ 0 & c_{sg22} & 0 & 0 & 0 & 0 \\ 0 & 0 & c_{sg33} & 0 & 0 & 0 \\ 0 & 0 & 0 & c_{sg44} & 0 & 0 \\ 0 & 0 & 0 & 0 & c_{sg55} & 0 \\ 0 & 0 & 0 & 0 & 0 & c_{sg66} \end{bmatrix} \tag{42}$$

where $c_{sg11} \equiv c_{sg22}$ and $c_{sg44} \equiv c_{sg55}$. Similarly, its normalized compliance matrix C_{SG_n} can be formulated (see details in [21]) as follows for non-dimensional comparison (Eq. 43):

$$C_{SG_n} = \begin{bmatrix} c_{sg_n11} & 0 & 0 & 0 & 0 & 0 \\ 0 & c_{sg_n22} & 0 & 0 & 0 & 0 \\ 0 & 0 & c_{sg_n33} & 0 & 0 & 0 \\ 0 & 0 & 0 & c_{sg_n44} & 0 & 0 \\ 0 & 0 & 0 & 0 & c_{sg_n55} & 0 \\ 0 & 0 & 0 & 0 & 0 & c_{sg_n66} \end{bmatrix} = \begin{bmatrix} \frac{c_{sg11}}{\frac{(2r_1+2d)^3}{EI_{m_z}}} & 0 & 0 & 0 & 0 & 0 \\ 0 & \frac{c_{sg22}}{\frac{(2r_1+2d)^3}{EI_{m_z}}} & 0 & 0 & 0 & 0 \\ 0 & 0 & \frac{c_{sg33}}{\frac{(2r_1+2d)^3}{EI_{m_z}}} & 0 & 0 & 0 \\ 0 & 0 & 0 & \frac{c_{sg44}}{\frac{(2r_1+2d)}{EI_{m_z}}} & 0 & 0 \\ 0 & 0 & 0 & 0 & \frac{c_{sg55}}{\frac{(2r_1+2d)}{EI_{m_z}}} & 0 \\ 0 & 0 & 0 & 0 & 0 & \frac{c_{sg66}}{\frac{2(r_1+2d)}{EI_{m_z}}} \end{bmatrix} \tag{43}$$

where we logically have $c_{sg_n11} \equiv c_{sg_n22}$ and $c_{sg_n44} \equiv c_{sg_n55}$ and $2r_1 + 2d$ is the characteristic length of the spring.

4.2.2. Geometric Optimization Strategy

As illustrated in Fig. 16, all the geometric parameters(r_1, θ_o, d, h and w), which can completely determine the geometric shape of the mechanism, are chosen to be studied for further mechanism optimization, in which position space concept is extended and not limited to positional parameters. The rest material properties are assigned in (44):

$$\begin{aligned} & E = 200 \times 10^9 \text{ Pa} \\ & \upsilon = 0.3 \end{aligned} \tag{44}$$

Logically, all elements in C_{SG_n} are the functions of the studied five parameters: r_1, θ_o, d, h and w, depending on which the process of improving the performance of the mechanism is logically deduced into a multi-variable (r_1, θ_o, d, h and w) and multi-objective (maximizing $\frac{c_{sg_n33}}{c_{sg_n22}}$, $\frac{c_{sg_n44}}{c_{sg_n66}}$, $\frac{c_{sg_n44}}{c_{sg_n22}}$ and $\frac{c_{sg_n33}}{c_{sg_n66}}$) optimization problem. c_{sg_n33} and c_{sg_n44}(and c_{sg_n55}) denote the translational compliance in Z direction and rotational compliance around X (Y) axis respectively while c_{sg_n22} (and c_{sg_n11}) and c_{sg_n66} stand for the translational compliance in Y (X) direction and rotational compliance around Z axis. Therefore, by maximizing $\frac{c_{sg_n33}}{c_{sg_n22}}$, $\frac{c_{sg_n44}}{c_{sg_n66}}$, $\frac{c_{sg_n44}}{c_{sg_n22}}$ and $\frac{c_{sg_n33}}{c_{sg_n66}}$ via Weighted-Sum Method [44], we aim to optimize the circular-beam-based Ortho-planar spring into a 2R1T (two rotational DOF and one translational DOF) compliant joint:

$$\begin{aligned} \max \quad & Z(r_1, \theta_o, d, h, w) = \epsilon_1 \frac{c_{sg_n33}}{c_{sg_n22}} + \epsilon_2 \frac{c_{sg_n44}}{c_{sg_n66}} + \epsilon_3 \frac{c_{sg_n44}}{c_{sg_n22}} + \epsilon_4 \frac{c_{sg_n33}}{c_{sg_n66}} \\ s.t. \quad & 0.010 \text{ m} \leq r_1 \leq 0.020 \text{ m} \\ & \pi/3 \leq \theta_o \leq 5\pi/9 \\ & 0 \text{ m} \leq d \leq 0.020 \text{ m} \\ & 0.0005 \text{ m} \leq h \leq 0.001 \text{ m} \\ & 0.001 \text{ m} \leq w \leq 0.003 \text{ m} \\ & r_1 + d \leq 0.020 \text{ m} \\ & d - w \geq 0.001 \text{ m} \\ & w - h \geq 0 \text{ m} \end{aligned}$$

where ϵ_1, ϵ_2, ϵ_3 and ϵ_4 are the weights of each single-optimized target respectively satisfying $\epsilon_1 + \epsilon_2 + \epsilon_3 + \epsilon_4 = 1$; $Z(r_1, \theta_o, d, h, w)$ is the objective function; Considering the importance of each objective, ϵ_1, ϵ_2, ϵ_3 and ϵ_4 are all set as $1/4$. The built-in Genetic Algorithm in MATLAB is used to obtain the globally optimal results with the following key parameters assigned: the population size is set up as 50; the number of maximum stall generations is assigned to 100; the random numbers generated within the bounds of the mentioned five variables are chosen as the initial population.

4.2.3. Globally Optimal Results with FEA Verification

The globally optimal result is listed in (45) with the corresponding consequent normalized compliance information obtained from the analytical models and FEA verification displayed in Table. 8 and the optimal geometric shape shown in Fig. 17a. According to Table. 8, the analytical results are verified by FEA results with maximum error being 11.29%. The values of $\frac{c_{sg_n33}}{c_{sg_n22}}$, $\frac{c_{sg_n44}}{c_{sg_n66}}$, $\frac{c_{sg_n44}}{c_{sg_n22}}$ and $\frac{c_{sg_n33}}{c_{sg_n66}}$ are up to around 200, 500, 1500 and 55 respectively, which implies that the optimal mechanism presents translational DOF in Z direction and rotational DOF around X and Y axes whereas it is translationally constrained in X and Y directions and rotationally constrained around Z axis. Therefore, the optimal circular-curved-beam-based Ortho-planar spring can serve as an ideal 2R1T compliant joint for many mechanical applications, such as continuum robots, rotational joints and springs.

- Globally Optimal Result

$$r_1 = 0.016 \text{ m};\ \theta_o = \frac{\pi}{2};\ d = 0.004 \text{ m};\ h = 0.0005 \text{ m};\ w = 0.003 \text{ m} \tag{45}$$

In the FEA, the boundary conditions were set up in the same manner of the analytical model where the compliance reference point of whole mechanism C_{SG} at $\mathrm{O_G}$ (Fig. 16) was evaluated (Fig. 17b): the motion stage and 3 links were set up as rigid bodies in COMSOL while the rest 6 compliant beams were set as deformable bodies (Fig. 17b); swept mapped meshes were used with the maximum and minimal mesh sizes being 0.02 mm and 2 mm respectively; the relative tolerance of the convergence error was set as 0.001 by default; only small deformations were considered so geometric non-linearity function was not activated; the geometric and material parameters were chosen from (44) and (45) respectively.

Table 8
Comparison between analytical results and FEA (without considering geometric non-linearity) results regarding the globally optimal Ortho-planar spring

Results	$c_{sg_n11}=c_{sg_n22}$	c_{sg_n33}	$c_{sg_n44}=c_{sg_n55}$	c_{sg_n66}	$\frac{c_{sg_n33}}{c_{sg_n22}}$	$\frac{c_{sg_n44}}{c_{sg_n66}}$	$\frac{c_{sg_n44}}{c_{sg_n22}}$	$\frac{c_{sg_n33}}{c_{sg_n66}}$
AM	3.4210×10^{-3}	6.4761×10^{-1}	5.4717×10^{0}	1.0973×10^{-2}	1.8930×10^{2}	4.9864×10^{2}	1.5994×10^{3}	5.9018×10^{1}
FEA	3.6094×10^{-3}	6.1393×10^{-1}	5.3395×10^{0}	1.1661×10^{-2}	1.7009×10^{2}	4.5789×10^{2}	1.4793×10^{3}	5.3149×10^{1}
ER	5.21%	5.48%	2.47%	5.90%	11.29%	8.90%	8.12%	11.04%

5. Conclusions

ICBs are good alternatives for mechanism synthesis as they provide many more diverse properties than straight flexible members. To fast synthesize ICB-based compliant mechanisms using screw theory, this paper proposed an efficient spatial compliance analysis method of general ICBs, by which the spatial compliance analysis of different types of ICBs (such as varying-curvature beams and varying-cross-section beams) was conducted, followed by Finite Element Analysis (FEA) verification. Next, the modeling and optimization of two types of CMs including ICB-based parallelogram mechanisms and ICB-based Ortho-planar springs were carried out under the concept of position space and parameter normalization strategy where a class of anti-buckling translational parallelograms with high load-bearing capacity and a type of compact 2R1T (2 rotational DOF and 1 translational DOF) compliant kinematic joints were obtained. Our future work will first include experimental testing of these proposed mechanisms. Then, the analysis of ICB-based mechanism in large-deformation situations will be conducted as this is what ICBs can stand out among other elementary flexible members. Third, we will promote and improve the used optimization strategy in nonlinear numerical solutions.

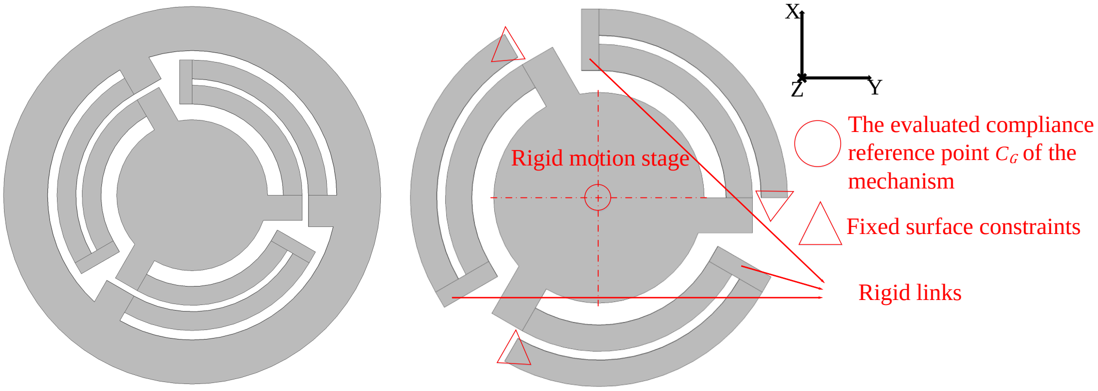

(a) The optimal geometric shape

(b) FEA verification boundary conditions

Figure 17: The optimal circular-curved-beam-based Ortho-planar Spring

Declaration of Competing Interest

The authors declare that they have no known competing financial interests or personal relationships that could have appeared to influence the work reported in this paper.

Acknowledgments

We would like to thank Haihong Li for introducing the basics of optimization theory and Shiyao Li for explaining the development of the analytical model.

References

[1] Larry L Howell. Compliant mechanisms. In 21st century kinematics. Springer, London, 2013.
[2] Nicolae Lobontiu. Compliant mechanisms: design of flexure hinges. CRC press, Boca Raton, 2020.
[3] D Farhadi Machekposhti, N Tolou, and JL Herder. A review on compliant joints and rigid-body constant velocity universal joints toward the design of compliant homokinetic couplings. Journal of Mechanical Design, 137(3), 2015.
[4] Haiyang Li, Guangbo Hao, and Richard C Kavanagh. Position-space-based compliant mechanism reconfiguration approach and its application in the reduction of parasitic motion. Journal of Mechanical Design, 138(9), 2016.
[5] Shixun Fan, Hua Liu, and Dapeng Fan. Design and development of a novel monolithic compliant xy stage with centimeter travel range and high payload capacity. Mechanical Sciences, 9(1):161, 2018.
[6] Guangbo Hao and Xianwen Kong. A novel large-range xy compliant parallel manipulator with enhanced out-of-plane stiffness. Journal of Mechanical Design, 134(6), 2012.
[7] Lin Cao, Allan T Dolovich, and Wenjun Chris Zhang. Hybrid compliant mechanism design using a mixed mesh of flexure hinge elements and beam elements through topology optimization. Journal of Mechanical Design, 137(9), 2015.
[8] Haiyang Li and Guangbo Hao. Position-space-based design of a symmetric spatial translational compliant mechanism for micro-/nano-manipulation. Micromachines, 9(4):189, 2018.
[9] Philipp Gräser, Sebastian Linß, Lena Zentner, and René Theska. On the influence of the flexure hinge orientation in planar compliant mechanisms for ultra-precision applications. In Proc. of the 59th International Scientific Colloquium, 59th Ilmenau Scientific Colloquium, Ilmenau, Germany, pages 1–10, 2017.
[10] Xin Dong, Mark Raffles, Salvador Cobos Guzman, Dragos Axinte, and James Kell. Design and analysis of a family of snake arm robots connected by compliant joints. Mechanism and Machine Theory, 77:73–91, 2014.
[11] G Palmieri, MC Palpacelli, and M Callegari. Study of a fully compliant u-joint designed for minirobotics applications. Journal of mechanical design, 134(11), 2012.
[12] Çağıl Merve Tanık, Volkan Parlaktaş, Engin Tanık, and Suat Kadıoğlu. Steel compliant cardan universal joint. Mechanism and Machine Theory, 92:171–183, 2015.
[13] Engin Tanık and Volkan Parlaktaş. Compliant cardan universal joint. Journal of mechanical design, 134(2), 2012.
[14] Guangbo Hao, Haiyang Li, Xiuyun He, and Xianwen Kong. Conceptual design of compliant translational joints for high-precision applications. Frontiers of Mechanical Engineering, 9(4):331–343, 2014.
[15] Ke Wu and Guangbo Hao. Design and nonlinear modeling of a novel planar compliant parallelogram mechanism with general tensural-compresural beams. Mechanism and Machine Theory, 152:1–23, 2020.
[16] Myeong-Gyu Song, Hyun-Woo Baek, No-Cheol Park, Kyoung-Su Park, Taeyong Yoon, Young-Pil Park, and Soo-Cheol Lim. Development of small sized actuator with compliant mechanism for optical image stabilization. IEEE Transactions on Magnetics, 46(6):2369–2372, 2010.

[17] Mostafa Abdalla, Mary Frecker, Zafer Gürdal, Terrence Johnson, and Douglas K Lindner. Design of a piezoelectric actuator and compliant mechanism combination for maximum energy efficiency. Smart materials and structures, 14(6):1421, 2005.

[18] Tanakorn Tantanawat, Zhe Li, and Sridhar Kota. Application of compliant mechanisms to active vibration isolation systems. In ASME 2004 International Design Engineering Technical Conferences and Computers and Information in Engineering Conference, pages 1165–1172. American Society of Mechanical Engineers Digital Collection, 2004.

[19] Brian Trease and Sridhar Kota. Design of adaptive and controllable compliant systems with embedded actuators and sensors. Journal of Mechanical Design, 131(11), 2009.

[20] Girish Krishnan and GK Ananthasuresh. Evaluation and design of displacement-amplifying compliant mechanisms for sensor applications. Journal of Mechanical Design, 130(10), 2008.

[21] Guangbo Hao and Xianwen Kong. A normalization-based approach to the mobility analysis of spatial compliant multi-beam modules. Mechanism and Machine Theory, 59:1–19, 2013.

[22] Ashok Kumar Rai, Anupam Saxena, and Nilesh D Mankame. Synthesis of path generating compliant mechanisms using initially curved frame elements. 129(10):1056–1063, 2007.

[23] Jin Qiu, Jeffrey H Lang, and Alexander H Slocum. A curved-beam bistable mechanism. Journal of microelectromechanical systems, 13(2):137–146, 2004.

[24] Y Gerson, S Krylov, B Ilic, and D Schreiber. Large displacement low voltage multistable micro actuator. In 2008 IEEE 21st International Conference on Micro Electro Mechanical Systems, pages 463–466. IEEE, 2008.

[25] Jeong Sam Han, Claas Müller, Ulrike Wallrabe, and Jan G Korvink. Design, simulation, and fabrication of a quadstable monolithic mechanism with x-and y-directional bistable curved beams. 19(2):1–6, 2007.

[26] Huy-Tuan Pham and Dung-An Wang. A constant-force bistable mechanism for force regulation and overload protection. Mechanism and Machine Theory, 46:899–909, 2011.

[27] Brian T Edwars, Brian D Jensen, and Larry L Howell. A pseudo-rigid-body model for functionally binary pinnedpinned segments used in compliant mechanisms. In Proceedings of the 1999 ASME Design Engineering Technical Conferences, 1999.

[28] Nianfeng Wang, Zhiyuan Zhang, Fan Yue, and Xianmin Zhang. Exploration of translational joint design using corrugated flexure units with bézier curve segments. Journal of Mechanical Design, 141(5), 2019.

[29] Horacio Ahuett-Garza, Oscar Chaides, Pedro N Garcia, and Pedro Urbina. Studies about the use of semicircular beams as hinges in large deflection planar compliant mechanisms. Precision Engineering, 38(4):711–727, 2014.

[30] Farid Parvari Rad, Rocco Vertechy, Giovanni Berselli, and Vincenzo Parenti-Castelli. Analytical compliance analysis and finite element verification of spherical flexure hinges for spatial compliant mechanisms. Mechanism and Machine Theory, 101:168–180, 2016.

[31] Farid Parvari Rad. Design and characterization of curved and spherical flexure hinges for planar and spatial compliant mechanisms. PhD thesis, University of Bologna, 2014.

[32] Giovanni Berselli, Farid Parvari Rad, Rocco Vertechy, and Vincenzo Parenti Castelli. Comparative evaluation of straight and curved beam flexures for selectively compliant mechanisms. In 2013 IEEE/ASME International Conference on Advanced Intelligent Mechatronics, pages 1761–1766. IEEE, 2013.

[33] Nianfeng Wang, Zhiyuan Zhang, Xianmin Zhang, and Chaoyu Cui. Optimization of a 2-dof micro-positioning stage using corrugated flexure units. Mechanism and Machine Theory, 121:683–696, 2018.

[34] John J Parise, Larry L Howell, and Spencer P Magleby. Ortho-planar linear-motion springs. Mechanism and machine theory, 36:1281–1299, 2001.

[35] Sushanta Ghuku and Kashi Nath Saha. Large deflection analysis of curved beam problem with varying curvature and moving boundaries. Engineering Science and Technology, an International Journal, 21(3):408–420, 2018.

[36] Zhichao Fan, Jian Wu, Qiang Ma, Yuan Liu, Yewang Su, and Keh-Chih Hwang. Post-buckling analysis of curved beams. Journal of Applied Mechanics, 84(3), 2017.

[37] M Jafari and MJ Mahjoob. An exact three-dimensional beam element with nonuniform cross section. Journal of applied mechanics, 77(6), 2010.

[38] Venkatasubramanian Kalpathy Venkiteswaran and Hai-Jun Su. Pseudo-rigid-body models for circular beams under combined tip loads. Mechanism and Machine Theory, 106:80–93, 2016.

[39] Venkatasubramanian Kalpathy Venkiteswaran and Hai-Jun Su. Pseudo-rigid-body models of initially-curved and straight beams for designing compliant mechanisms. In International Design Engineering Technical Conferences and Computers and Information in Engineering Conference, volume 5A. American Society of Mechanical Engineers, 2017.

[40] Nianfeng Wang, Xiaohe Liang, and Xianmin Zhang. Pseudo-rigid-body model for corrugated cantilever beam used in compliant mechanisms. Chinese Journal of Mechanical Engineering, 27(1):122–129, 2014.

[41] Shorya Awtar and Shiladitya Sen. A generalized constraint model for two-dimensional beam flexures: Nonlinear strain energy formulation. Journal of mechanical Design, 132(8), 2010.

[42] Guimin Chen, Fulei Ma, Guangbo Hao, and Weidong Zhu. Modeling large deflections of initially curved beams in compliant mechanisms using chained beam constraint model. Journal of Mechanisms and Robotics, 11(1), 2019.

[43] Mingxiang Ling, Larry L Howell, Junyi Cao, and Guimin Chen. Kinetostatic and dynamic modeling of flexure-based compliant mechanisms: a survey. Applied Mechanics Reviews, 72(3), 2020.

[44] Kalyanmoy Deb. Multi-objective optimization. In Search methodologies, pages 403–449. Springer, 2014.

[45] Earl William Swokowski. Calculus with analytic geometry. Taylor & Francis, 1979.

[46] Warren Clarence Young, Richard Gordon Budynas, Ali M Sadegh, et al. Roark's formulas for stress and strain, volume 7. McGraw-Hill, New York, 2002.

[47] Guimin Chen and Larry L Howell. Two general solutions of torsional compliance for variable rectangular cross-section hinges in compliant mechanisms. Precision Engineering, 33(3):268–274, 2009.

[48] Shiyao Li, Guangbo Hao, and William MD Wright. Design and modelling of an anti-buckling compliant universal joint with a compact configuration. Mechanism and Machine Theory, 156:104–162, 2021.

[49] C Qiu, P Qi, HB Liu, Kaspar Althoefer, and Jian S Dai. Six dimensional compliance analysis of ortho-planar springs for a continuum manipulator. In International Design Engineering Technical Conferences and Computers and Information in Engineering Conference, volume 138, page 51. American Society of Mechanical Engineers, 2014.

[50] Guangbo Hao. Design and analysis of symmetric and compact 2r1t (in-plane 3-doc) flexure parallel mechanisms. Mechanical Sciences, 8(1):1–9, 2017.

[51] Guangbo Hao, Jingjun Yu, and Yufei Liu. Compliance synthesis of a class of planar compliant parallelogram mechanisms using the position space concept. In 2018 International Conference on Reconfigurable Mechanisms and Robots (ReMAR), pages 1–10. IEEE, 2018.

[52] Shorya Awtar, Kevin Shimotsu, and Shiladitya Sen. Elastic averaging in flexure mechanisms: A three-beam parallelogram flexure case study. Journal of Mechanisms and Robotics, 2(4), 2010.

[53] Shorya Awtar and Alexander H Slocum. Closed-form nonlinear analysis of beam-based flexure modules. In ASME 2005 International Design Engineering Technical Conferences and Computers and Information in Engineering Conference, pages 101–110. American Society of Mechanical Engineers Digital Collection, 2005.

[54] Shorya Awtar, Alexander H Slocum, and Edip Sevincer. Characteristics of beam-based flexure modules. Journal of Mechanical Design, 129(6), 2007.

[55] Pier Paolo Valentini and Eugenio Pezzuti. Computer-aided tolerance allocation of compliant ortho-planar spring mechanism. International Journal of Computer Applications in Technology, 53(4):369–374, 2016.

[56] Olivier Smal, Bruno Dehez, Benoît Raucent, Michaël De Volder, Jan Peirs, Dominiek Reynaerts, Frederik Ceyssens, Johan Coosemans, and Robert Puers. Modelling, characterization and testing of an ortho-planar micro-valve. Journal of Micro-Nano Mechatronics, 4(3):131–143, 2008.

[57] Harris Kristanto, Prathamesh Sathe, Chincheng Hsu, Alexander Schmitz, Tito Pradhono Tomo, Sophon Somlor, and Shigeki Sugano. Development of a 3-axis human fingertip tactile sensor with an ortho-planar spring. In 2019 IEEE International Conference on Robotics and Biomimetics (ROBIO), pages 297–302. IEEE, 2019.

[58] Jelizaveta Konstantinova, Agostino Stilli, and Kaspar Althoefer. Fingertip fiber optical tactile array with two-level spring structure. Sensors, 17(10):2337, 2017.

[59] Asghar Ataollahi, Arash Soleiman Fallah, Lakmal D Seneviratne, Prokar Dasgupta, and Kaspar Althoefer. Novel force sensing approach employing prismatic-tip optical fiber inside an orthoplanar spring structure. IEEE/ASME Transactions on Mechatronics, 19(1):121–130, 2012.

[60] Craig P Lusk. Ortho-planar mechanisms for microelectromechanical systems. PhD thesis, Brigham Young University, 2005.

[61] Peng Qi, Hongbin Liu, Lakmal Seneviratne, and Kaspar Althoefer. Design, kinematics and prototype of a flexible robot arm with planar springs. In International Design Engineering Technical Conferences and Computers and Information in Engineering Conference. American Society of Mechanical Engineers, 2015.

[62] Peng Qi, Chen Qiu, Hongbin Liu, Jian S Dai, Lakmal D Seneviratne, and Kaspar Althoefer. A novel continuum manipulator design using serially connected double-layer planar springs. IEEE/ASME Transactions on Mechatronics, 21(3):1281–1292, 2015.

[63] Peng Qi, Chen Qiu, Hongbin Liu, Jian S Dai, Lakmal Seneviratne, and Kaspar Althoefer. A novel continuum-style robot with multilayer compliant modules. In 2014 IEEE/RSJ International Conference on Intelligent Robots and Systems, pages 3175–3180. IEEE, 2014.

Highlights

Efficient Spatial Compliance Analysis of General Initially Curved Beams for Mechanism Synthesis and Optimization

Ke Wu,Gang Zheng,Guangbo Hao

- We proposed an efficient compliance analysis method of initially curved beams
- We validated the method using Finite Element Analysis
- We conducted compliance analysis and optimization of ICB-based mechanisms
- We used weighted-sum method and genetic algorithm for the optimization process